Appendix.

Appendix A1: The validity of several methods used in downscaling simulations

As described in Chapter 5, there are several issues that should be considered in the experimental setup or methods used in Chapter 5. These issues are (1) the validity of the size distribution of regenerated aerosol particles, and (2) the method to determine the initial and lateral boundary condition for SDF of hydrometeors.

The size distribution of regenerated aerosol particles is determined by eq. (2-5), which is based on Feingold et al. (1996), but the validity of this equation should be tested because the equation was originally developed for idealized simulation with a periodic lateral boundary condition.

The nesting method used in Chapter 5 assumes that there are no clouds but a super saturated air mass, whose relative humidity is determined by the total water mixing ratio of domain II of Chapter 5, at initial time and lateral boundary of domain III. This method can affect the simulated results.

In the following section we consider these issues.

A1.1. Validity of the parameterization of Feingold et al. (1996)

First, we discuss the validity of SDF of regenerated aerosol. In this study, we implement the regeneration process of aerosol by complete evaporation of vapor, and two types of parameterization give the size distribution of regenerated aerosols.

The first type assumes that SDF of regenerated aerosol particles is same as initial SDF of aerosol particles (henceforth we refer to this parameterization as "I-SDF"), the other type gives SDF of regenerated aerosol particles by eq. (2-5), which is developed by Feingold et al. (1996). The eq. (2-5) is based on the concept that the radius of regenerated aerosol particles is larger than that of aerosols before they activate.

The parameterization of Feingold et al. (1996) is used only for experiments in Chapter 3 and 4 (*i.e.*, the idealized experiment with periodic boundary condition), and the I-SDF parameterization is used for experiments in Chapter 5 and 6 (*i.e.*, the downscaling simulation), because the parameterization of Feingold et al. (1996: henceforth we refer to as F96 parameterization) is not valid for downscaling simulation. We show, in this section, the reason that F96 parameterization is not valid for downscaling simulation.

To show the reason, we conduct the downscaling simulations whose experimental setup is same as downscaling simulations in Chapter 5 except for the parameterization of SDF of regenerated aerosol. We use both type of the parameterizations.

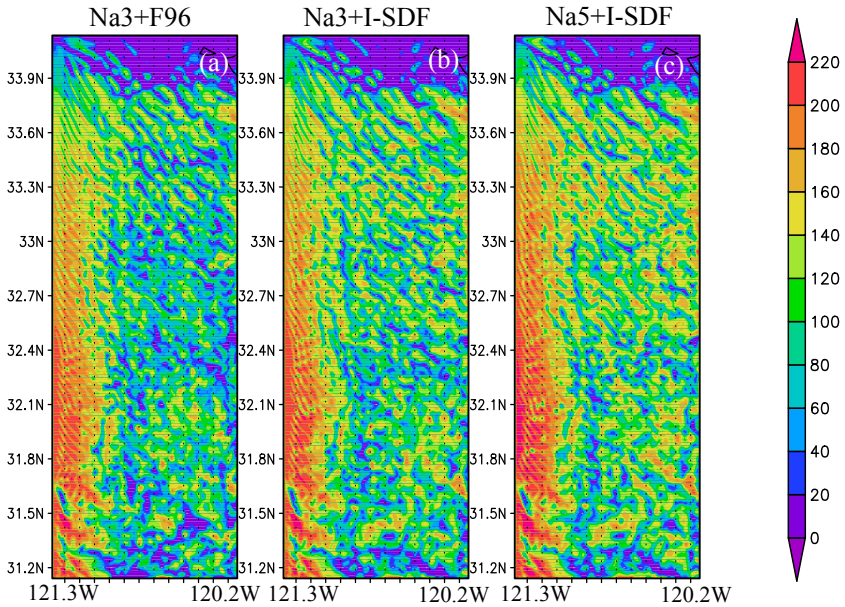

Figure A1.1. Simulated radiance [$Wm^{-2}Sr^{-1}m^{-1}$] at λ=0.62 μm with (a) Na3 and F96 parameterization, (b) Na3 and I-SDF parameterization, and (c) Na5 and I-SDF parameterization, respectively, at 15 UTC on 10 of July 1987.

The radiance at 15 UTC on July 10, 1987 simulated by the model with each parameterization are shown in Fig. A1.1. It is found that radiance simulated by using F96 parameterization is smaller than that by using I-SDF parameterization.

For understanding the reason of this small radiance, we check the domain-averaged SDF of aerosol just above cloud top, shown in Fig. A1.2. It is seen from the figure that the large amount of coarse aerosol particles (*i.e.*, $r_a > 1$ μm) is simulated by F96 parameterization.

In addition, the rainfall simulated by F96 parameterization is lager than that by I-SDF parameterization (figure not shown).

From these results, it is seemed that the large aerosol particles generated by the regeneration process make large cloud droplets by activation. The large cloud droplets can easily grow to raindrop, which results in large amount of surface rainfall and optically thin clouds. From this result, we can conclude that F96 parameterization is not valid for downscaling simulation.

Although we show the invalidity of F96 parameterization, we must consider the reason of the invalidity. To investigate the reason, we reconsider the equation of F96 parameterization shown as:

$$R_k(t) = N(t)\frac{\phi_k(t)}{\sum_{k=1}^{n_a}\phi_k(t)}, \quad \phi_k(t) = \frac{\bar{N}_k(0) - \bar{N}_k(t)}{\bar{N}_k(0)}, \tag{A1-1}$$

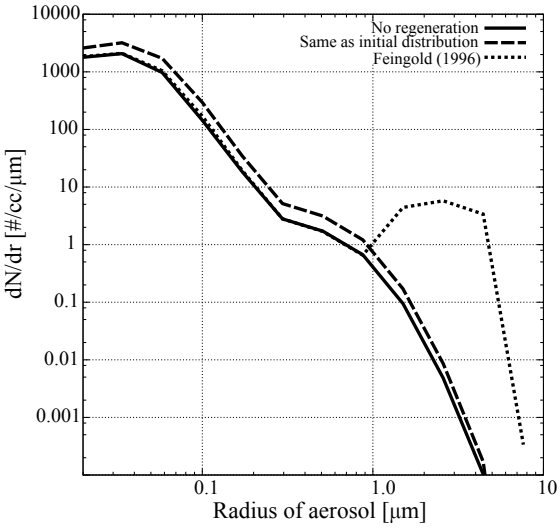

Figure A1.2. Number density (SDF) of aerosol just below the cloud base simulated (solid line) without regeneration, (dashed line) with regeneration through the parameterization by which SDF of regenerated aerosols are given as the same SDF of initial time, (dotted line) with regeneration through the parameterization of Feingold et al. (1996), respectively, averaged over domain III at 15 UTC on July 10, 1987.

where $\overline{N}(t)$ is the domain-averaged number concentration of aerosol particles at time t, $N(t)$ is the total number concentration of regenerated aerosol particles at time t, n_a is the number of aerosol bins, and $R_k(t)$ is the number concentration of regenerated aerosol at the k-th aerosol bin at time t.

It is appeared that the size distribution of regenerated aerosol is determined by domain-averaged number concentration of aerosol at initial time and that at time t. The smaller the number concentration of k-th bin at a time t is, the larger the amount of regenerated aerosol of k-th bin is.

In downscaling simulation, the number concentration of large aerosol particles near the upstream lateral boundary at a time t is always smaller than that at initial time, because coarse aerosol particles are activated in super saturated air mass. In addition, coarse particles, which are produced by regeneration process, flow out from calculation domain at downstream lateral boundary.

In this situation, the amount of coarse aerosol particles in calculation domain is small in downscaling simulation. Thus, unnaturally large aerosol particles are always produced by regeneration process calculated by F96 parameterization.

In idealized simulation with horizontally periodic lateral boundary condition (*i.e.*, experimental setup of section 3 and 4), coarse aerosol particles produced by regeneration process can stay in calculation domain. Thus, unnaturally large amount of coarse aerosol particles are not generated by the regeneration process.

From these results, we can conclude that the F96 parameterization can be used only for idealized simulation with horizontally periodic boundary conditions, but it is not valid parameterization for

downscaling simulation as shown in Chapter 5.

A1.2. Comparison of size distribution of aerosol simulated by 1D-SBM, 2D-SBM and obtained by in situ measurement

In the previous chapter, we investigate the validity of size distribution of regenerated aerosol (SDRA). As well as the verification, it is useful to compare observed SDRA with model derived SDRA.

Although the comparison is useful, it is very difficult to determine whether observed aerosol has been regenerated or not, because of device limitation. To overcome this difficulty, multi-dimensional spectral bin models, which can trace aerosols explicitly in cloud droplets, was developed by some previous studies (*e.g.* Chen and Lamb, 1994; Xue et al., 2011; MD-SBM).

Following the previous studies, we extend the 1D SBM used in this study to 2D SBM, which explicitly traces aerosols in cloud droplets. In this section, we describe the comparison of 1D SBM with 2D SBM.

Since the computational cost of the 2D SBM is much larger than 1D SBM, we perform a downscaling simulation as shown in Chapter 5 but with a smaller size domain targeting the DYCOMS-II period when the aircraft observations were conducted.

The experimental setup is mostly same as that in Chapter 5 except for domain size and targeting day. The calculation domains and nesting information are shown in Fig. A1.3. The detail of the experimental set up is shown in Table A1.1.

The initial and boundary conditions of dynamical properties (*i.e.* wind velocity, potential temperature, vapor mixing ratio, and SST) of domain I_a are nested from JRA-25 for every 6 hours. Orographic data are obtained from GTOPO30. The initial and boundary conditions of domain II_a (domain III_a) is nested from results of domain I_a (domain II_a) for every 2 hours (1 hour).

In domain III_a, we perform simulation by using both 1D SBM and 2D SBM for the comparison. Initial and lateral boundary conditions for SDFs of hydrometeors are assumed to zero (*i.e.*, no cloud) as mentioned in Chapter 5. Aerosols are only calculated for domain III_a. A horizontally uniform aerosol field, whose chemical species is assumed to be sulfate, is used in domain III_a.

The SDFs of aerosols are based on aircraft measurement represented in Fig. A1.4. Since the measurement data of aerosols obtained from aircraft are available only below and above cloud, the SDFs of aerosol in cloud layer are given by interpolating observed SDFs of aerosol above and below clouds. The regeneration process of 1D-SBM is calculated by F96 parameterization Details of the model setup are shown in Table A1.1.

Table A1.1. Catalog of the numerical experiment

	domain I_a *4	domain II_a *4	domain III_a *4
Dynamics	NHM*5	NHM*5	NHM*5
Microphysics	BULK*1	BULK*1	BIN*2
Aerosol	X*6	X*6	OBS*3
Horizontal grid spacing	5 km	2 km	500 m
Domain size (horizontal)	1515x1515km^2	404x404km^2	75x37.5km^2
Vertical grid spacing	10~350m	5~220m	5~60m
Vertical grid number	60	80	60
Model top height	10165m	8885m	1915m
Turbulence Scheme	WF*7	WF*7	DD*7
Initial and boundary condition	JRA	$NHM10_a$ *8	$NHM2_a$ *8
Calculation time (dt)	168 h (10s)	60 h (2s)	6h (0.5s)
Sampling interval of nesting	6h	3h	2h
Start time	2001/7/5/12UTC	7/9/18UTC	7/11/06UTC

*1: BULK means bulk microphysical model (Yamada, 2003)

*2: BIN means spectral bin microphysical model (Khain et al., 2000; HUCM)

*3: OBS means aerosol field based on aircraft measurement

*4: Domain I_a, II_a, and III_a are shown in Fig. A1.3

*5: NHM means the dynamical framework (Saito et al., 2006)

*6: X means the experiment did not implement the process

*7: WF means turbulence scheme used for weather forecasting, and DD is that of Deadroff (1980)

*8: $NHM10_a$ and $NHM2_a$ indicate experiments with 10 km and 2 km grid spacing, respectively.

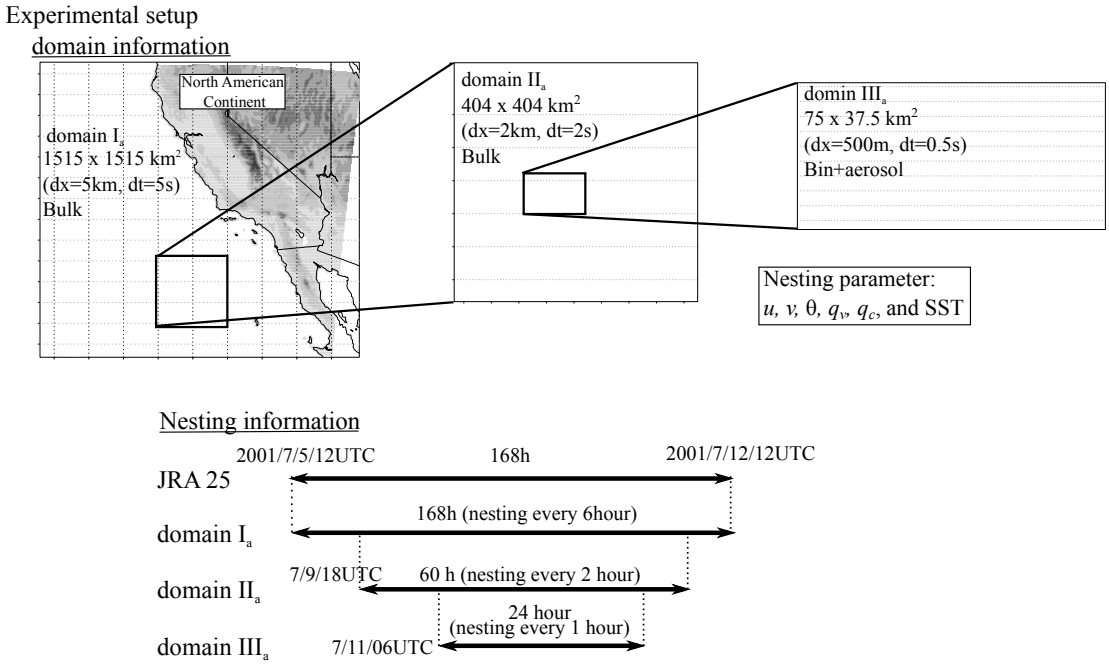

Figure A1.3. Experimental setup of downscaling simulation in chapter A1.2 and A1.3

Because cloud-top height (CTH; corresponding to PBL height) of NHM10$_a$ underestimates that obtained from observation, we raise the PBL height by changing profiles of the potential temperature and vapor mixing ratio when the boundary and initial condition of domain III$_a$ are nested. This treatment can make artificial gravity waves or an inertial wave, but the effects of the waves are negligible after a few hours from starting time of domain III$_a$ calculation (figure not shown). To avoid errors by these waves and spin-up, we analyze the results at 11UTC on 2001 July 11, when it is 5 hours after the start time of domain III$_a$ calculation.

The data used for the comparison is obtained from the observation conducted by C130 aircraft of Research Aviation Factory of National Center for Atmospheric Research (NCAR/RAF), whose flight path and time series of altitude are shown in Fig. A1.5.

The aircraft boarded several instruments to observe the size distribution of aerosols: A PMS Passive Cavity Aerosol Spectrometer Probe (PCASP), which measures aerosol particles with diameters of 100 nm to 3 μm, and Model 300 of Forward Scattering Spectrometer Probe (FSSP-300), which measures aerosol particle, whose diameters are from 300 nm to 20 μm, are used to obtain the SDFs of aerosols.

Since these two instruments cannot distinguish between cloud droplets and aerosol particles, the SDFs of aerosols are only obtained below cloud bottom or above the cloud top. Among these SDFs of aerosols, we use SDFs of aerosols above the cloud top for comparison because the entrainment,

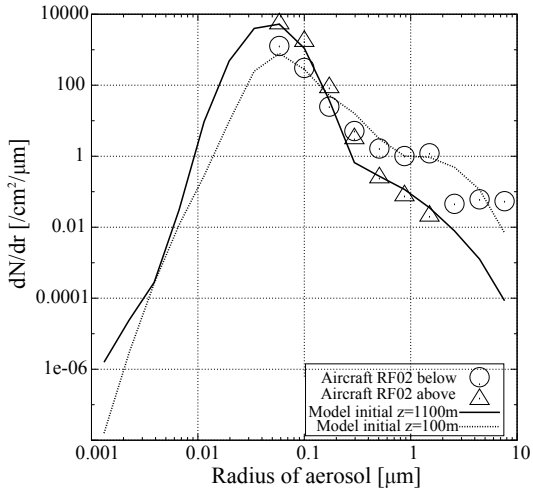

Figure A1.4. SDFs of aerosol (circle, triangle) observed by aircraft and (solid, dotted line) assumed initial and latreal boundaries under the condition of (circle, dotted line) below clouds z=100m, and (trianble, solid line) above clouds z=1100m.

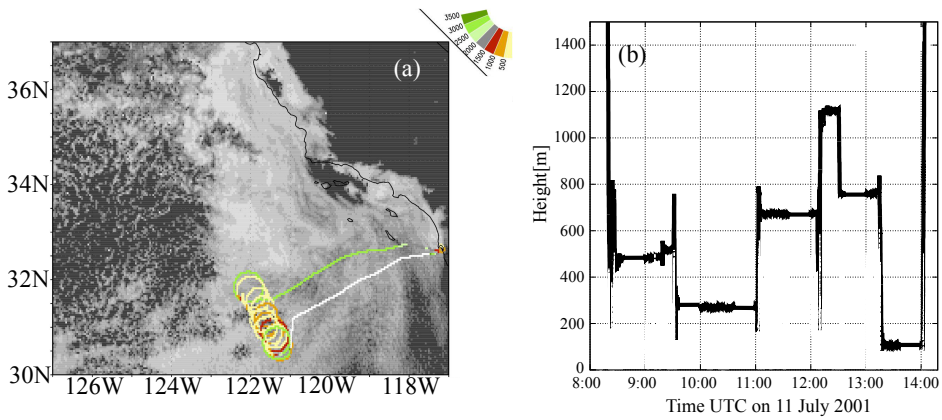

Figure A1.5. Flight path of C130 aircraft of RF02 during the DYCOMS-II field campaign. (a) Geophysical distribution of albedo (obtained from eq. (3-8) and CAPCOM retreival algorithm) with colored lines, which shows flight height (m), and (b) time series of flight altitude

evaporation and regeneration occur more frequently.

The COT and RE used for the comparison are retrieved from GOES-10 satellite by using the Comprehensive Analysis Program for Cloud Optical Measurement (CAPCOM; Nakajima and Nakajima, 1995; Kawamoto et al., 2001) algorithm.

Before we compare model results with observation results, we show the computational time (CPU time) of 1D and 2D SBM. Since the difference of these two models is the cloud microphysics scheme, the CPU times of the cloud microphysics scheme are measured.

Table A1.2. Computational (CPU) time of cloud microphysics 15 minutes from starting time of each calculation

	CPU times [s]
1D-SBM	1454.85
2D-SBM	29214.49

Table A1.2 shows the CPU times of the models to calculate the 15 minutes from starting time of the simulations. It is seen from this table that the CPU time of 2D-SBM is 20 times larger than that of 1D-SBM, and calculation cost of 2D-SBM is too large for us to conduct several sensitivity experiments.

Figure A1.6 shows spatial distribution of COT retrieved from satellite and simulated by the 1D-SBM. Although the model does not reproduce a detailed structure of clouds, it roughly reproduces the COT obtained from satellite. This result justifies the model results for the comparison with observed results. Figure A1.7 shows SDF of aerosols observed from C130 aircraft, simulated by 1D-SBM, and 2D-SBM.

The SDFs of aerosols simulated by 1D-SBM without the regeneration process underestimates the number concentration of aerosol particles larger than 0.2 μm. The reason for this underestimation is discussed in Chapter 5 and Fig. 5.8.

The SDF of aerosols simulated by 1D-SBM with the regeneration process overestimates number concentration of large aerosol particles, suggesting that the amounts of large size aerosols produced by the regeneration process are too large, although the regeneration process is needed to maintain reasonable number concentrations of cloud droplets in the model. The reason of this over estimation

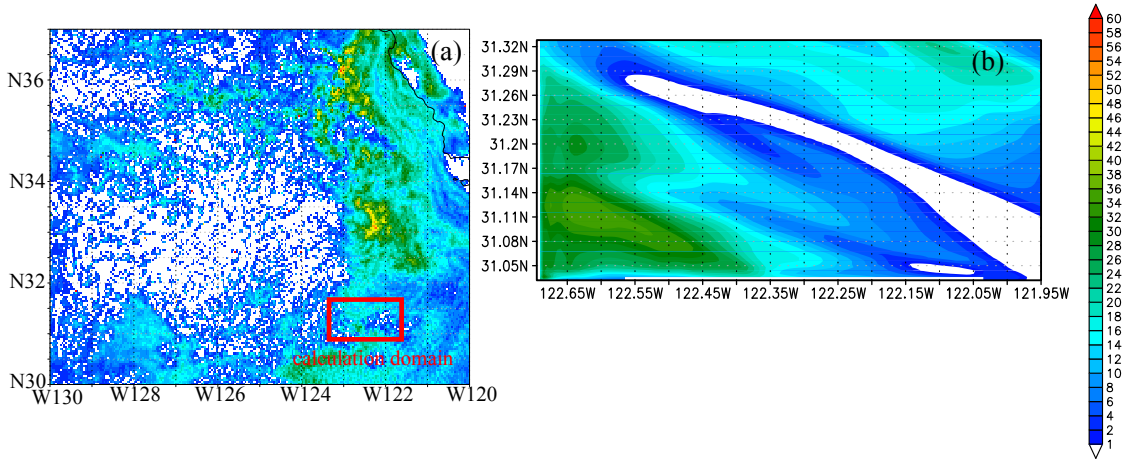

Figure A1.6. Cloud optical thickness at 11UTC on 11 July 2001 (a) retrieved from GOES-10 satellite with a square, which corresponds to calculation domain, and (b) simulated by the model.

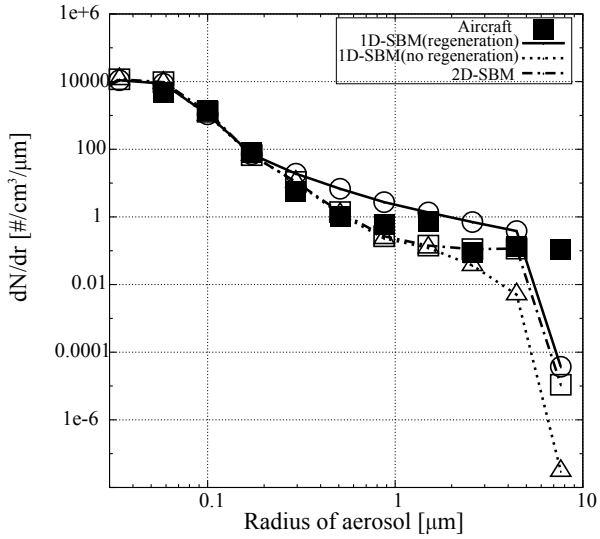

Figure A1.7. Size distribution of aerosol above the cloud top simulated by (dash-dotted line with open square) 2D-SBM, (solid line with open circle) 1D-SBM with the regeneration process, (dotted line with open triangle) 1D-SBM without the regeneration process, and (closed square) obtained from C130 aircraft in situ measurement.

is discussed in the previous section.

The SDF of aerosols obtained by 2D-SBM underestimates the number concentration of large particles. These results mean that the SDFs of aerosols cannot be reproduced by the regeneration process alone, and other sources are needed to reproduce observed aerosol size distributions. We will discuss other sources of aerosols in Appendix A2.

A1.3. Initial and lateral boundary conditions for SDF of hydrometeors

Secondly, we investigate the effects of the initial and lateral boundary SDFs of hydrometeors and conducted additional sensitivity experiments, of which initial and lateral boundary condition for SDFs are given by a gamma distribution. Experimental setup is same as that of the previous section. The SDFs of initial boundary condition are given by an equation as shown in Pruppacher and Klett (1997):

$$f(r) = A_g r^2 \exp\left(-B_g r\right) \qquad \text{(A1-2)}$$

where f is the number density concentration of cloud (SDF) and r is radius of hydrometeors. A_g, and B_g are given by the equations shown as follows:

$$A_g \approx 1.45 \times 10^{-6} \left(\frac{LWC}{\rho_w \bar{r}^6} \right), \qquad \text{(A1-3)}$$

$$B_g = \frac{3}{\bar{r}}, \qquad \text{(A1-4)}$$

where $\bar{r}$ is average radius, which is assumed to be 1 μm in this study, ρ_w is density of water (unit is g cm^{-3}). The $\bar{r}$ value is determined through additional sensitivity experiments (figure not shown). LWC of initial and lateral boundary is nested from the model result of domain II_a.

We also conduct the several sensitivity experiments shown below. Firstly, sensitivity experiment of SDF for lateral boundary condition is conducted. We conduct same simulation without cloud but super saturated air mass at lateral boundary (referred to as CNTLA) and with cloud, of which SDFs are given by eq. (A1-2) (referred to as CNTLA-nest).

Secondly, the sensitivity experiments of aerosol amount are conducted. The aerosol amounts are changed from the value of CNTLA, to the value, of which the number concentration of aerosol is 100 times smaller than CNTLA value (henceforth we refer to NA001-nest). For this sensitivity experiments, initial and boundary condition of SDF for clouds are given by eq. (A1-2).

To investigate the sensitivity to PBL height, thirdly, the experiments of 200 m lower PBL height (henceforth we refer to HA-200-nest experiment) is also conducted. We change PBL heignt by changing profile of potential temperature and vapor mixing ratio when we nest from domain II_a to domain III_a. The initial and boundary condition for SDF of clouds are given by eq. (A1-2)

Figure A1.8 shows the spatial distribution of COT simulated by the sensitivity experiments, and the PDF of COT is represented in Fig. A1.9. It is found that COT simulated with the lateral and initial SDFs of hydrometeors (*i.e.* COT simulated by CNTLA-nest, NaA001-nest, and HA-200-nest experiments) is thinner than that simulated without the lateral and initial SDFs of hydrometeors (*i.e.* COT simulated by CNTLA experiments).

It is seemed that the reason of thin COT simulated with the lateral SDFs of hydrometeor is attributed to the low relative humidity of the lateral boundary. The vapor mixing ratio of CNTLA experiment is given by the total water mixing ratio of domain II_a, which corresponds to a super saturated air mass.

This super saturated air mass makes nucleation process active, which results in optically thick cloud. The vapor mixing ratio of the other experiments is given by the vapor mixing ratio of domain II_a and liquid water mixing ratio is used to give the lateral SDFs given by the eq. (A1-2), which corresponds to lower relative humidity than that of CNLA experiments. In this condition, nucleation of cloud droplets is not active, as a result, optically thin clouds are generated.

Figure A1.10 indicates the RE-COT pattern obtained from CNTLA-nest, NaA001-nest, and HA-200-nest experiments. Figures A1.10a and A1.10c indicate that the trend of the RE-COT pattern

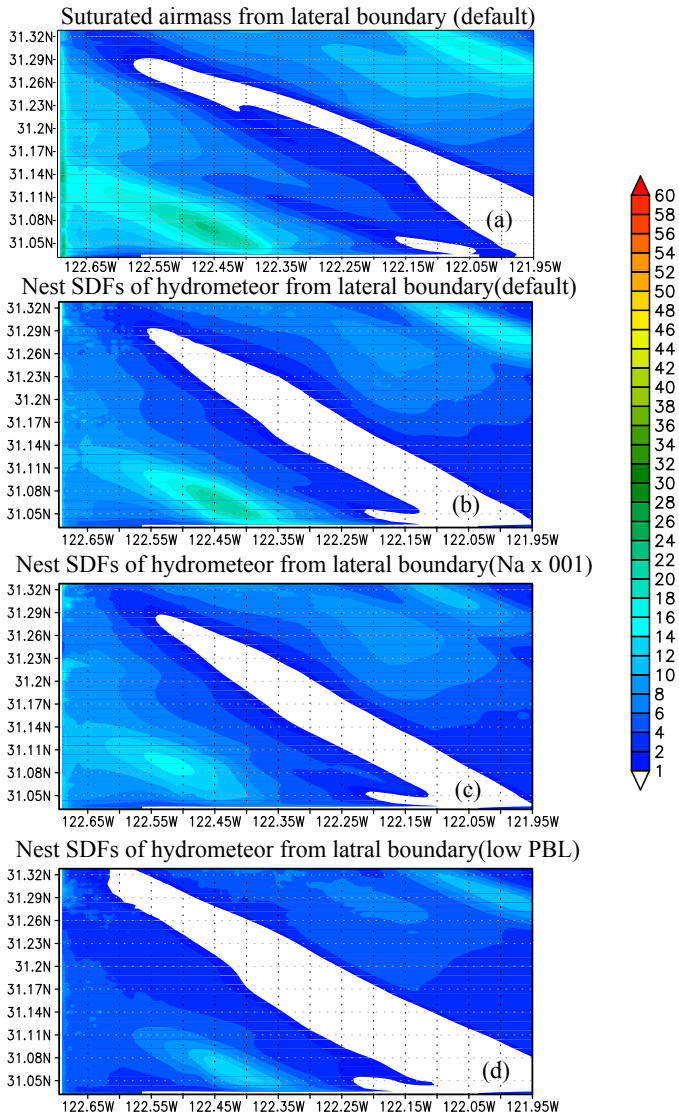

Figure A1.8 Spatial distributions of Cloud optical thickness (COT τ_c) at 11 UTC on 11 July of 2001 obtained from (a) CNTLA, (b) CNTLA-nest, (c) NaA001-nest, and (d) HA-200-nest experiments.

obtained from the sensitivity experiment changing PBL height is the same as that obtained from the same kind of experiments as shown in Chapter 5.

A comparison of Fig. A1.10a and A1.10b indicates that the RE-COT pattern reproduced by "NaA001-nest" experiments located in the upper and more left area than that reproduced by "CNTLA-nest" experiment, although the difference of the two figures is small. We can concluded that the trend of the RE-COT pattern obtained from the sensitivity experiment changing aerosol amount is same as that obtained from the same kind of experiment as shown in Chapter 5.

The small difference between CNTLA-nest and NaA001-nest experiment results from aerosol particles generated by regeneration process. The cloud droplets originating from the lateral boundary

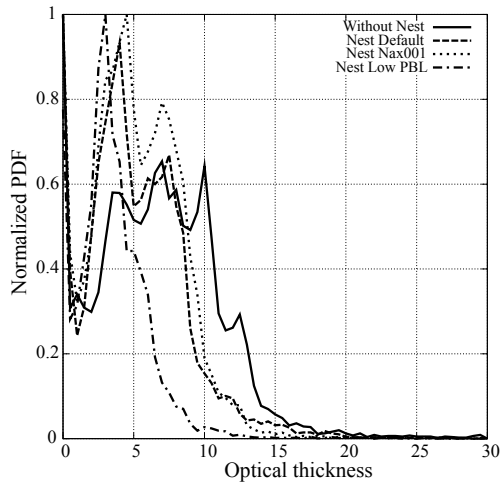

Figure A1.9. Normalized PDF of COT (τ_c) obtained from (solid line) CNTLA, (dashed line) CNTLA-nest, (dotted line) NaA001-nest, and (dot-dashed line) HA-200-nest experiments, respectively.

gives additional aerosol into the calculation domain by the regeneration process, and make an air mass with a relatively large amount of aerosols.

From these results, we can conclude that the initial and lateral condition for SDFs of hydrometeors is one of the factors that can affect the microphysical properties of simulated cloud. In spite of the effect, the trend of RE-COT patterns, the target of this study, is same regardless of the method to give the initial and lateral boundary SDF of hydrometeors. This conclusion justifies the results obtained from the experiments conducted in Chapter 5.

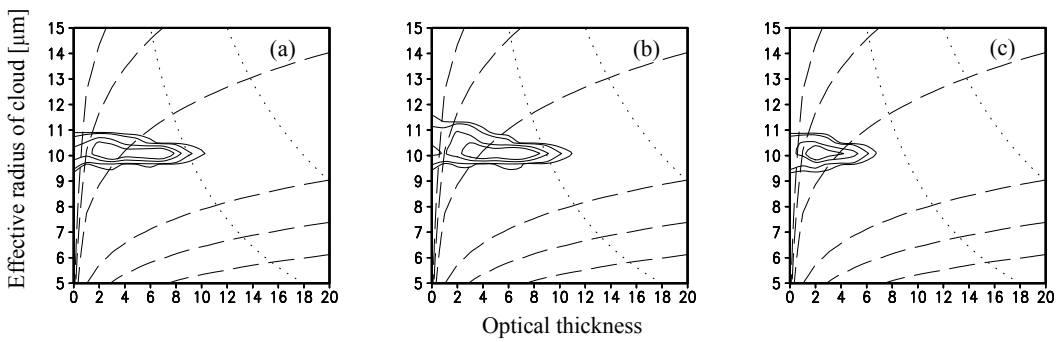

Figure A1.10 Correlation patterns between r_{eff} and τ_c over the center of domain III obtained from (a) CNTLA-nest, (b) NaA001-nest, and (c) HA-200-nest experiments, respectively. The contour values are set to 0.05, 0.1, 0.3, 0.5, with the maximum value of 1. The dotted and dashed curves are isolines of cloud number concentration N_c and liquid water path W, respectively, based on an adiabatic model. The isolines are for N_c = 30, 50, 100, 300, 500, and W = 50, 100 g m^{-2}

Appendix A2: Regeneration and other sources

In Chapter 5, we insist that the regeneration process of aerosol is needed to supply aerosol particles for the model atmospheres to reproduce the characteristics of RE-COT patterns.

However simulations by 2D-SBM indicate that the regeneration is not enough to reproduce aerosol distribution observed by in situ aircraft measurement. Recently, some studies (*e.g.* Kazil et al., 2011) reported that other sources could supply aerosols for real atmosphere. We introduce these sources of aerosol in this section.

Aerosol sources of the marine boundary layer (MBL) have been reported in a large amount of previous studies. Katoshevski et al. (1999) and Clarke et al. (2006) reported the emission of sea salt aerosol from the sea surface and aerosol inflow above the MBL by entrainment. Heintzenberg et al. (2004) reported that aerosol nucleation (*i.e.* gas to particle conversion) is one of the potential sources of aerosol in the marine boundary layer. Several studies also reported strong correlation between aerosol concentration of MBL and dimethyl sulfide (DMS) emitted from the sea surface (Ayers and Gras, 1991; Andrea et al., 1995; Clarke et al., 1998).

In addition, aerosol inflow from the South American continent in the VAMOS Ocean-Cloud-Atmosphere-Land Study Regional Experiment (VOCALS-REx) observation campaign and its importance are reported (Carmichael, 2011, personal communication).

These sources are summarized in Fig. A2.1. Since the model used in this study considers only

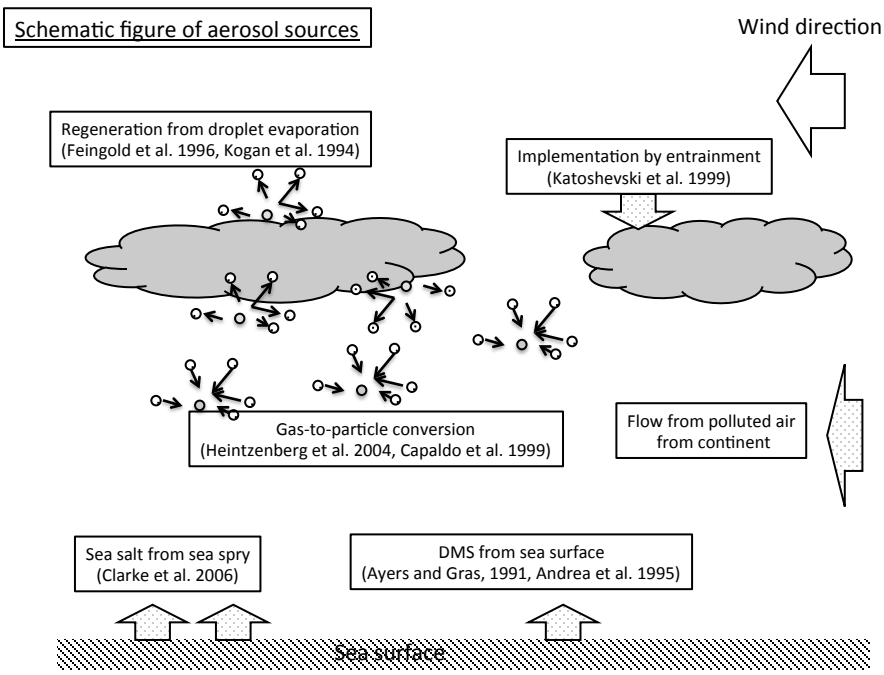

Figure A2.1. Schematic illustration of aerosol sources in marine boundary layer

"regeneration of aerosol", and "aerosol inflow", as mentioned, this issue must be improved upon by implementing aerosol emission from the sea surface, and by using a chemical transport model in future.

Appendix A3: Basic equations of the dynamical core of JMA-NHM

In this section, we show the basic equations of the dynamical core of JMA-NHM as general information of the model used in this study. In JMA-NHM, fully compressible equations considering a map factor are adopted as the basic equations (Saito, 1997). The momentum equations are given as flux form:

$$\frac{\partial}{\partial t}\left(\frac{\rho u}{m_f}\right)+Adv.\left(\frac{\rho u}{m_f}\right)+\frac{\partial p}{\partial x}=Crv.\left(\frac{\rho u}{m_f}\right)+Cor.\left(\frac{\rho u}{m_f}\right)+Dif.\left(\frac{\rho u}{m_f}\right), \qquad \text{(A3-1)}$$

$$\frac{\partial}{\partial t}\left(\frac{\rho v}{m_f}\right)+Adv.\left(\frac{\rho v}{m_f}\right)+\frac{\partial p}{\partial y}=Crv.\left(\frac{\rho v}{m_f}\right)+Cor.\left(\frac{\rho v}{m_f}\right)+Dif.\left(\frac{\rho v}{m_f}\right), \qquad \text{(A3-2)}$$

$$\frac{\partial}{\partial t}\left(\frac{\rho w}{m_f}\right)+Adv.\left(\frac{\rho w}{m_f}\right)+\frac{1}{m_f}\left(\frac{\partial p}{\partial z}+\rho g\right)=Crv.\left(\frac{\rho w}{m_f}\right)+Cor.\left(\frac{\rho w}{m_f}\right)+Dif.\left(\frac{\rho w}{m_f}\right), \qquad \text{(A3-3)}$$

$$m_f=\left(\frac{\cos\varphi}{\cos\varphi_1}\right)^{c-1}\left(\frac{1+\sin\varphi_1}{1+\sin\varphi}\right)^{c};\quad c=\left(\frac{\cos\varphi_1}{\cos\varphi_2}\right)/\ln\left(\frac{\tan\left(\frac{\pi}{4}-\frac{\varphi_1}{2}\right)}{\tan\left(\frac{\pi}{4}-\frac{\varphi_2}{2}\right)}\right), \qquad \text{(A3-4)}$$

where u, v, and w are zonal, meridional, and vertical wind velocity, respectively, p is pressure, g is gravitational acceleration, ρ is density including hydrometeors; m_f is defined as the map factor, φ_1 and φ_2 are the standard latitudes, and φ is the latitude. *Adv.*, *Crv.*, *Cor.*, and *Dif.* show the advection, curvature, Coriolis, and diffusion process, respectively. The thermodynamic equation is given as follows:

$$\frac{\partial\theta}{\partial t}+Adv.\theta=\frac{Q}{C_p\Pi}+Dif.\theta, \qquad \text{(A3-5)}$$

$$\Pi=\left(\frac{p}{p_0}\right)^{R_v/C_p}, \qquad \text{(A3-6)}$$

where θ is the potential temperature, Q is the diabatic heating rate, C_p is the specific heat of dry air at constant pressure, Π is defined as exner function, p_0 is standard pressure and R_v is gas constant for dry air. The continuity equation is given as,

$$\frac{\partial\rho}{\partial t}+m_f^2\left\{\frac{\partial}{\partial x}\left(\frac{\rho u}{m_f}\right)+\frac{\partial}{\partial y}\left(\frac{\rho v}{m_f}\right)\right\}+\frac{\partial}{\partial z}(\rho w)=Prc., \qquad \text{(A3-7)}$$

where *Prc.* is the term corresponding to the gravitational settling of the hydrometeors.

The basic conservation equation of hydrometeors is given as

$$\frac{\partial f_{i,k}}{\partial t} + Adv.\left(f_{i,k}\right) - Drp.\left(f_{i,k}\right) = -\left[\frac{\partial f_{i,k}}{\partial t}\right]_{microphysics}, \qquad \text{(A3-8)}$$

where $f_{i,k}$ is SDF of hydrometeors in size bin category whose subscripts i and k denote the type of hydrometeors and bin number. The term $[]_{microphysics}$ is the change of SDF by cloud microphysical process. The detailed equations of cloud microphysics are shown in Chapter 2 of this paper, Iguchi et al. (2008), and Sato et al. (2009).

Appendix A4: Estimation of CPU time of the model

In Chapter 4, we discussed the effects of horizontal grid resolution for the microphysical structure simulated by the model. The purpose of the discussion is to estimate the effects and to justify the downscaling simulation assuming real atmosphere by coarse grid resolution (*i.e. dx*=500m).

Although it is easy to infer that CPU time of the simulation with fine grid resolution is huge, we should show the CPU times to calculate the simulations; therefore, we estimate the CPU time in this chapter.

To estimate the CPU times, we conduct the experiments during 3.5 minutes, whose experimental setups are same as Chapter 4. The experiments are conducted with changing grid resolution (*i.e.* amount of grids) without changing the amount of processors (*i.e.* 15 processors), which is used for the parallel computation. The experiments are also conducted with changing amount of processors with constant grid resolution (*i.e.* 22500 grids for horizontal grid; 150x150x75 grids). The Hitachi SR16000 of the Research Institute of Information Technology, Kyushu University is used for the calculation.

Figure A4.1 shows CPU times to calculate during 3.5 minutes integration. Figure A4.1a shows that CPU times increase in proportion to amounts of grids, and Fig. A4.1b shows that CPU times reduced exponentially with decreasing number of processors. Although we conduct calculations in a short time with large amount of processors, 128 processors are the most efficient for calculation, considering waiting times, which is the time from the times when we submit jobs to the times when the jobs are started.

If the waiting time is not considered, a rough estimation based on the results shown above indicates that it takes about 160 days to calculate the simulations conducted in Chapters 5 and 6 with fine grid resolution (*i.e.* dx=50m; 2500 x 6000 x 60 grids, and 6 hour time integration). Since the

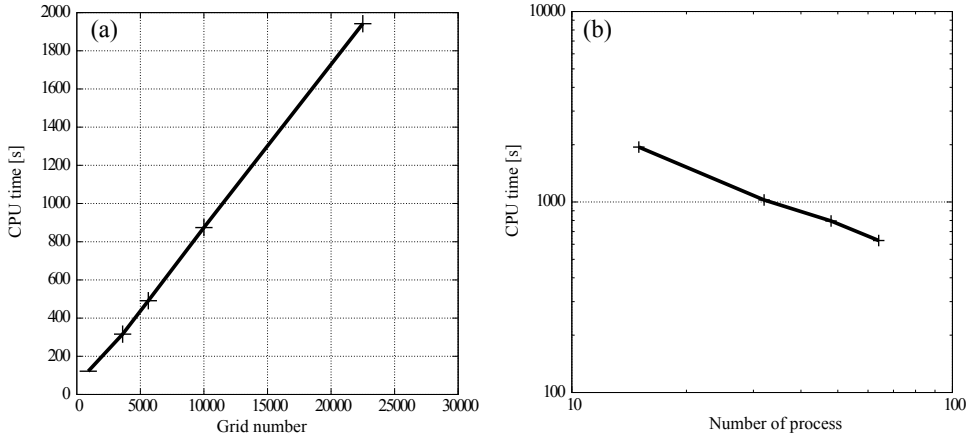

Figure A4.1. CPU time to calculate 3.5 minutes time integration assuming the experimental setup same as that of chapter 4 (a) by using 15 processors, and (b) with 22500 grids (150x150 grids for horizontal domain).

real time including the waiting time for calculation is much longer than the estimated time, the calculation with fine grid is not possible in the present study. However, we must conduct the same simulation with finer grid resolution in future.

Appendix A5: Factors determining general characteristics of CFODD

Since the characteristics of CFODD are not investigated in Chapter 6, we investigate factors to determine the characteristic of CFODD through results of the sensitivity experiment. Although previous studies (N10, S10, and Sato et al., 2012b) characterized CFODD through the three modes (*i.e.* condensation mode, collision mode, and evaporation mode), the bimodality of hydrometeor's SDF in each area on CFODD is useful to define the characteristic of CFODD, because it roughly represents how many cloud droplets are in collision growth process. We, therefore, investigate the sensitivity of the bimodality to aerosol amounts and PBL height.

Figure A5.1 represents scatter plots between the rate of clouds, of which the SDFs have the bimodal distribution, and the PBL height, column CN number concentration. It appears that both PBL height and aerosol amount correlate to rate of bimodality. Clouds, whose SDF have bimodal distribution, increase with increasing (decreasing) PBL height (aerosol amount). These results indicate that cloud droplets can easily grow to a large size in unstable or pristine conditions. Although both PBL height and aerosol amount affects the rate of bimodality, PBL height correlates more with bimodality. The correlation coefficient of PBL height and aerosol amount with bimodality is 0.812 and -0.508, respectively. From the results, we can conclude that the higher (smaller) the PBL height (aerosol amount) is, the more clouds have bimodal distribution of SDF, and that PBL height mainly determines the rate of bimodality and the aerosol amount also affect the rate but it is a

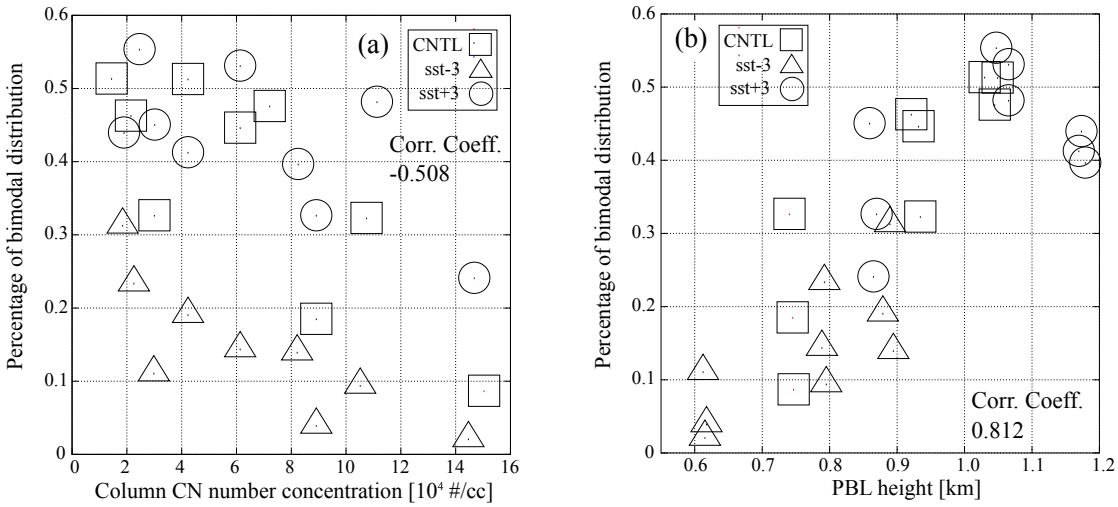

Figure A5.1 Scatter plots (a) between bimodality and PBL height, (b) between bimodality and column CN number concentration. Square, circle, and triangle plots are the results obtained from CNTL, SST-3, and SST+3 experiments, respectively.

secondary factor. As we describe in Chapter 3, clouds, whose SDF take bimodal distribution, locate in areas whose radar reflectivity is larger than 10 *dBZe* regardless of RE and COD. The results in Chapter 3 and the result in Fig. A5.1 indicate that higher PBL and smaller aerosol amount can make CFODD locate to the right and bottom area of each category.

Although the results indicate one of the possible factors determining the CFODD, we must investigate in future the effects of other factors, which can change the pattern.

Appendix A6: Notations of symbols used in this paper

We summarize notations of symbols used in this paper in Table A6.1.

Table A6.1 Notations of symbols used in this paper

Symbols	Meaning
A, B	Used in eq. (2-1)
A_g, B_g	Used in eq. (A1-2)~(A1-3)
A_{lb}	Cloud Albedo
A_1, A_2, A_3	Mode fraction used in eq. (2-4)
A_{cg}	Used in eq. (A9-8)~(A9-9)
a	Used in eq. (3-1)
C_p	Specific heat of dry air at constant pressure
C_{bk}	Backscattering cross section
$c_{w,k}$	Used in eq. (A8-5)
$c_{a,p}$	Used in eq. (A8-15), (A8-16)
$D_{drizzle}$	Drizzling rate
D_v	Diffusivity of water vapor
D_{LS}	Large scale divergence (=3.75 x 10^{-6} s^{-1})
E_{coll}	Collision efficiency
E_{coal}	Coalescence efficiency
$E_{collection}$	Collection efficiency
e_w	Saturation vapor pressure over water
F	Used in eq. (2-2)
F_r, F_0, F_1	Used in eq. (3-1)
f	Number concentration (SDF) of cloud droplets
f'	Used in eq. (A8-5)
f_a	Number concentration (SDF) of aerosol particles
g	Gravitational accelaration
g_c	Mass distribution function (SDF) of cloud droplets
g'_c, $\tilde{g}$	Used in eq. (A8-5)
H_c	Geometrical depth of the cloud

H_v	Heaviside step function
h	Height
K	Collection kernel given as eq. (2-3)
K_r	$\lvert K_r \rvert = \lvert (m_r^2 - 1)/(m_r^2 + 2) \rvert$
K_α	Thermal conductivity of air
k_a	Coefficients relating the volume-mean radius to the effective radius ($k_a^{-1/3}$=1.1)
L_w	Specific latent heat of vaporization
L_{MCI}	Number of random number used by Monte Carlo integration to select type of hydrometeors
l_a	Adiabaticity factor
M_{CCN}	Molecular weight of the aerosol
M_{spc}	Number of aerosol chemical species
M_{MCI}	Number of random number used by Monte Carlo integration to select bin
m	Mass of cloud droplets
m_a	Mass of aerosol particles
m_c	Used in (A8-3)
m_f	Map factor
m_r	Complex refractive index
N_{aero}	Number of aerosol bin (*i.e.*, 13 or 17)
N_{bin}	Number of cloud bin (*i.e.*, 33)
N_c	Cloud number concentration
N_m	Number of modes in eq. (2-4)
$\bar{N}_k(t)$	Domain averaged number concentration of aerosol at time t
N_t	A threshold value of N_c
$N_{c,\,max}$	Maximum value of N_c on RE-COT patterns
N_{spr}	Aerosol number concentration nested from SPRINTARS
N_{spc}	Number of hydrometeors type
n_a	Number of aerosol bins

p	Pressure
p_0	Standard pressure
Q	Diabatic heating rate
Q_r	Used in eq. (3-1)
Q_{ext}	Extinction coefficient
q_l	Used in eq. (3-1)
$R_k(t)$	Regenerated aerosol number concentration of *k-th* aerosol bin
R_v	Gas constant of vapor
R_{comp}	Reduction rate of calculation amount by Monte Carlo integration
r	Radius of cloud droplets
r_a	Radius of aerosol particles
r_{crit}	Critical radius of aerosol in nucleation process
r_{max}	Maximum radii of cloud droplets in the model
r_{min}	Minimum radii of cloud droplets in the model
r_{eff}	Cloud-droplet effective radius (RE)
r_v	Volume radius
r_1, r_2, r_3	Mode radius of aerosol particles
$r_{2.1}$, $r_{3.7}$	2.1, 3.7 μm channel-retrieved cloud-droplet effective radius
$\bar{r}$	Average radius
S_w	Supersaturation over water
T	Temperature
t	Time
u, v, w	Wind valocity
u_*	Friction velocity (=0.25 m s^{-1})
V	Terminal velocity of cloud droplets
W	Liquid water path
$Wmax$	Maximum value of liquid water path
w_{LS}	Large scale subsidence
w_λ	Weight function given in Platnick (2000)

w_{MCI}, w'_{MCI}	Weight function used in Monte Carlo integration
x_c, y_c	Used in eq. (A8-5)
Z_e	Radar reflectivity
$Z_{e,true}$	True radar reflectivity
z, Δz	Altitude, Grid interval of altitude
z_{top}, z_{bottom}, z_{model_top}	Cloud top, Cloud bottom, Model top
α	Used in eq. (3-12)~(3-17)
β	Used in eq. (A8-5)
ϕ	Used in eq. (2-5)
η	Prognostic variable
φ, φ_1, φ_2	Latitude, Standard latitude
κ	Used in eq. (3-1)
λ	Wavelength
ν	Van't Hoff factor
Π	Exner function
θ	Potential temperature
ρ	Air density
ρ_i	Used in eq. (3-1)
ρ_w	Water density
ρ_{ccn}	Density of aerosol
$\sigma_{ext,ra}$	Extinction coefficient
σ_1, σ_2, σ_3	Geometrical standard deviatioin
τ_c	Cloud optical thickness (COT)
τ_d	Cloud optical depth (COD)
τ_t	Used in eq. (3-6)
ζ	ln(m)
ζ_c, ζ_1	Used in eq. (A8-3)
σ_{MCI}, μ_{MCI}, ν_{MCI}, λ_{MCI}	Represent the type of hydrometeor

Appendix A7: Discussion on a threshold value of RE (RE=14μm) suggested by the previous study

One of the targets of this thesis is to study the characteristics of RE-COT pattern, and some interesting suggestion about the RE used in RE-COT pattern reported in previous studies (*e.g.*, Rosenfeld and Gutman, 1994). Their suggestion was that RE=14 μm retrieved from AVHRR satellite is the threshold value for precipitating/non-precipitation cloud.

In the study of evolution of cloud, the particle size associated with precipitation is important, therefore it is interesting to investigate the relationship between the threshold value and RE-COT pattern. We discuss the relationship in this section.

As we have discussed in Chapter 5, the transition from condensation process to collision process is represented as the change from positive correlation to negative correlation of RE-COT pattern. The transition point corresponds to right vertex of each anticlockwise triangle in Figure 5.12a.

Figure A7.1 shows trajectories of clouds as shown in Fig. 5.12a but with the other two trajectories and the line of the threshold value (*i.e.*, RE=14μm). It is found that the value of RE at transferring points (*i.e.*, right vertex of each triangle) of most of the experiments are larger than the threshold value or nearly equal to it. These trajectories are obtained from the simulation at 500 m grid resolution.

While, there are two trajectories whose value of RE do not exceed the threshold value. The shape of these trajectories is not a triangle (*i.e.*, there are no transfer point from condensation to collision), and only the positive correlation is shown. The trajectories are obtained from the clouds simulated by the 50 m grid resolution.

Based on the analysis of Chapter 5, the results show that precipitation (or drizzling) occurs in most of the clouds except for the two clouds. The drizzle rate of each experiment, in which the trajectory of clouds in the RE-COT plain shows triangle shape, is same order as that of heavy drizzling cloud observed by aircraft in situ measurement (*e.g.*, van Zanten et al., 2005) as shown in Table 4.1.

While, drizzle rate of the experiments, in which the trajectory of clouds does not show triangle, is 0.00965 mm day^{-1} as shown in Table 4.1, which is same order as that of non drizzling clouds measured by the aircraft observation.

These results demonstrate that drizzle particles generate in the clouds whose trajectories on RE-COT plane is anticlockwise triangle form, and the value of RE at the transferring points of each clouds exceed the threshold value as shown by previous study (*i.e.*, RE=14 μm).

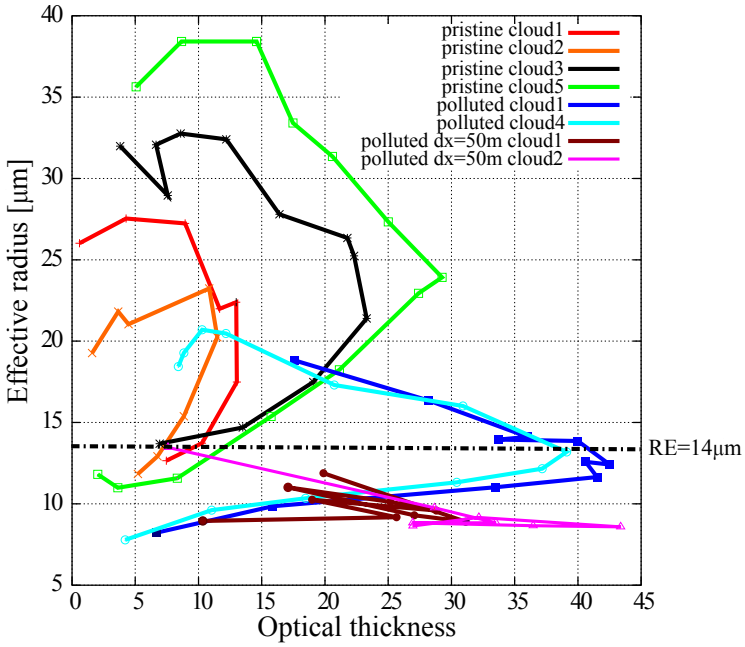

Figure A7.1 Same as Figure 6.11a but with trajectories of clouds in polluted experiment simulated by the model of 50 m grid resolution. The solid lines show the trajectories of each cloud, the dotted-dashed line shows threshold line of RE=14μm

The results also demonstrate that drizzling does not occur in the clouds whose trajectories is not a triangle shape but only positive correlation pattern are shown, in addition, the RE of these clouds does not exceed the threshold value.

These result support the suggestion of the previous study that the value of RE=14 μm is the threshold value of drizzling.

Appendix A8: Description of Monte Carlo integration applied for stochastic collection equation (SCE) and two-dimensional spectral bin model (2D-SBM)

In this paper, we applied Monte Carlo integration method developed by Sato et al. (2009) to stochastic collection equation (SCE) shown as eq. (2-3), and extend the one-dimensional spectral bin model (1D-SBM) to 2D-SBM to calculate size distribution of aerosol particles in cloud droplets. We describe the detail of the Monte Carlo integration and 2D-SBM in this section.

A8.1. Monte Carlo integration of stochastic collection equation

The Monte Carlo integration method for SCE is developed by Sato et al. (2009) to conduct SCE calculation with small computational cost. The SCE is given as eq. (2-3) and as:

$$\frac{\partial f(m)}{\partial t} = \int_0^{\infty} f(m)K(m,m')f(m')dm' - \int_0^{m/2} f(m-m'')K(m,m'')f(m'')dm''$$
$$K(m,m') = \pi\{r(m)+r'(m')\}|V(m)-V(m')|E_{coll}(m,m')E_{coal}(m,m') \quad , \qquad \text{(A8-1)}$$

where m is mass of cloud droplets, f is number density (SDF) of hydrometeors, V is terminal velocity, E_{coll} and E_{coal} represent collision efficiency, and coalescence efficiency, respectively. In order to solve eq. (A8-1), logarithmically equidistant mass grid system following Bott (1998) is adopted. Following Berry (1967), a mass density function, $g_c(\zeta)$, is introduced by

$$g_c(\zeta) = m^2 f(m), \qquad (\zeta = \ln m). \qquad \text{(A8-2)}$$

Substituting $g_c(\zeta)$ into eq.(A8-1), the SCE of the mass density function is written as:

$$\frac{\partial g_c(\zeta)}{\partial \zeta} = 2\int_0^{\zeta_1} \frac{m^2}{m_c^2 m'} g(\zeta')g_c(\zeta_c)K(\zeta',\zeta_c)d\zeta' - \int_0^{\infty} g_c(\zeta)\frac{K(\zeta,\zeta'')}{m''}g_c(\zeta'')d\zeta'' , \qquad \text{(A8-3)}$$

where $\zeta_c = \ln(m_c)$; $m_c = m - m'$; $\zeta_1 = \exp(\zeta)/2$.

Collision of a particle at a grid point i (i-th bin), whose mass is m_i, with a particle at a grid point j (j-th bin), whose mass is m_j, yields a change in the mass density functions at the i-th and j-th bins, $g_{c,i}$ and $g_{c,j}$. It also products a new particle with mass $m' = m_i + m_j$. This process is calculated as follows:

$$g_{c,i}(i,j) = g_{c,i} - g_{c,i}\frac{K(i,j)}{m_j}g_{c,j}\Delta\zeta\Delta t = g_{c,i} - \Delta g_{c,i}, \qquad \text{(A8-4a)}$$

$$g_{c,j}(i,j) = g_{c,j} - g_{c,j}\frac{K(i,j)}{m_i}g_{c,i}\Delta\zeta\Delta t = g_{c,j} - \Delta g_{c,j}, \qquad \text{(A8-4b)}$$

$$g'_c(i,j) = \Delta g_{c,i} + \Delta g_{c,j}, \quad (i,j = 1,2,\ldots N_{bin}), \qquad \text{(A8-4c)}$$

where $\Delta g_{c,i}$, $\Delta g_{c,i}$ are the masses lost from i-th and j-th bins by collision, respectively, and $g_{c,i}(i,j)$ and $g_{c,j}(i,j)$ are values of the mass density function after the collision at the i-th and j-th bin. N_{bin} is number of hydrometeor bins (*i.e.*, 33 bins). $g'_c(i,j)$ represents the total mass increase of the particle

system identified as the new particle m' after the collision. $\Delta\zeta$ is the grid spacing of the logarithmically equidistant mass grid system. Δt is the time interval for numerical integration.

Supposing that the new particle mass is in a k-th bin, (*i.e.*, $m_k < m' < m_{k+1}$), $g'_c(i,j)$ is decomposed into two contributions for k-th and $k+1$-st bins as in the scheme proposed by Bott (2000), which is shown as:

$$
\begin{aligned}
g'_{c,k}(i,j) &= g_{c,k} + g'_c(i,j) \\
g_{c,k}(i,j) &= g'_{c,k}(i,j) - f'_{c,k+1/2}(i,j) \\
g_{c,k+1}(i,j) &= g_{c,k+1} + f'_{c,k+1/2}(i,j) \\
f'_{c,k+1/2}(i,j) &= \frac{g'_c(i,j)}{g'_{c,k}(i,j)} \int_{1/2-c_{w,k}}^{1/2} \tilde{g}_{c,k}(x_c)\,dx_c \\
&= \frac{g'_c(i,j)}{\beta}\left[\exp\left(\frac{\beta}{2}\right) - \exp\left\{\frac{\beta}{(1/2-c_{w,k})}\right\}\right], \qquad \text{(A8-5)} \\
c_{w,k} &= \frac{\ln m' - \ln m_k}{\ln m_{k+1} - \ln m_k} \\
\tilde{g}_{c,k}(x_c) &= g'_{c,k}(i,j)\exp(\beta x_c) \\
\beta &= \frac{\ln g_{c,k+1}}{\ln g'_{c,k}(i,j)}, \quad x_c = \frac{y_c - y_{c,k}}{\Delta y_c}, \quad y_c = \ln r
\end{aligned}
$$

where r is radius of hydrometeors.

Traditional bin method evaluates all the collision combination ${}_{Nbin}C_2$, to solve (A8-3) as follows:

$$
\left\{g_{c,l}\right\}_{l=1,2,\cdots N_{bin}} = \sum_{i}^{N_{bin}-1}\sum_{j}^{N_{bin}}\left(\Delta g_{c,i} + \Delta g_{c,j}\right). \qquad \text{(A8-6)}
$$

On the other hand, the Monte Carlo integration (MCI) algorithm does not calculate all combination of bins, instead only some combinations are selected by using uniform random numbers:

$$
\left\{g_{c,l}\right\}_{l=1,2,\cdots N_{bin}} = \sum_{k_1,k_2=1}^{M_{MCI}}\left(\Delta g_{c,k_1} + \Delta g_{c,k_2}\right)\times w_{MCI}, \quad w_{MCI} = \frac{{}_{N_{bin}}C_2}{M_{MCI}}, \qquad \text{(A8-7)}
$$

where M_{MCI} is number of selected bin combinations and w_{MCI} is weighting factor to compensate for the lack of mass changed caused by the reduced number combinations. Computational efficiency is improved by introducing the factor w_{MCI} compared to the traditional bin method.

Eqs. (A8-1), (A8-3), (A8-6), and (A8-7) assume collision and coagulation among particles of the same type of hydrometeor. We can extend these expressions to those for poly dispersions for different types of hydrometeors, such as the seven hydrometeor types identified in the UT-ACBM as follow:

$$\frac{\partial f^{(\lambda_{MCI})}(m)}{\partial t} = \sum_{\nu_{MCI}} \sum_{\mu_{MCI}} \int_0^{\infty} f^{(\nu_{MCI})}(m) K(m,m') f^{(\mu_{MCI})}(m') dm' - \sum_{\sigma_{MCI}} \int_0^{m/2} f^{(\lambda_{MCI})}(m-m'') K(m,m'') f^{(\sigma_{MCI})}(m'') dm'' , \quad \text{(A8-8)}$$

$$\left\{ g_{c,l}^{(\lambda_{MCI})} \right\}_{l=1,2,\cdots N_{bin}}^{\lambda_{MCI}=1,2,\cdots N_{spc}} = \sum_{\mu_{MCI}} \sum_{\nu_{MCI}} \left[\sum_i \sum_j \left(\Delta g_{c,i}^{(\mu_{MCI})} + \Delta g_{c,j}^{(\nu_{MCI})} \right) \right]$$

$$\approx \sum_{\lambda_{MCI,1}=1,\lambda_{MCI,2}=1}^{L_{MCI}} \sum_{k_1=1,k_2=1}^{M_{MCI}} \left[\left(\Delta g_{c,k_1}^{(\lambda_{MCI,1})} + \Delta g_{c,k_2}^{(\lambda_{MCI,2})} \right) \right] \times w'_{MCI} , \quad \text{(A8-9)}$$

$$w'_{MCI} = \frac{{}_{N_{bin}}C_2}{M_{MCI}} \frac{N_{spc}^2}{L_{MCI}}$$

where μ_{MCI}, ν_{MCI}, σ_{MCI}, and λ_{MCI} represent the type of hydrometeor, N_{spc} is the number of hydrometeor types and L_{MCI} is the number of hydrometeor types selected in the MCI.

The quadruples integration in eq. (A8-8) is reduced to a double summation in (A8-9), so that the MCI introduces a significant benefit in the calculation time for the collision-coagulation process for poly dispersions including different types of hydrometeors.

In summary, the computational efficiency is improved by random bin selection with ratio of w_{MCI} ($= {}_{Nbin}C_2/M_{MCI}$) and also by hydrometeor type selection with ratio of w'_{MCI} ($=N^2_{spc}/L_{MCI}$). The total computation time is therefore reduced by the factor $R_{comp}=1/w_{MCI}w'_{MCI}$.

In case of large w_{MCI}, the size distribution in the next time step can become negative when $g_{c,i} < \Delta g_{c,i}$ or $g_{c,j}<\Delta g_{c,j}$. In this case, we assume positive definiteness by the following procedure as proposed by Bott (1998):

$$g_{c,i}(i,j) = \max\left(g_{c,i} - \Delta g_{c,i}, 0\right)$$
$$g_{c,j}(i,j) = \begin{cases} \max\left(g_{c,j} - \Delta g_{c,j}, 0\right) & (i \neq j) \\ g_{c,j} - \Delta g_{c,j} & (i = j) \end{cases} . \quad \text{(A8-10)}$$

Our method is also different from traditional bin method in terms of calculation order regarding hydrometeor types and sizes of hydrometeor. Traditional bin methods calculate interaction of different hydrometeor types and different sizes by collision with specific order (*e.g.*, first, collision of liquid drop and ice particle, second liquid drop and snow particle, next liquid drop and graupel *etc.*). This can be invalid for collision process in nature if the natural collision processes occurs randomly in terms of paring of colliding particles and types. In our MCI, however, collision process is calculated by random order about hydrometeor type and size of hydrometeor because the order is selected by using uniform random number. This may be more suitable to represent the stochastic nature of collision process in real clouds.

A8.2. Extension of one-dimensional SBM to two-dimensional SBM

Extension of 1D-SBM to 2D-SBM is one of the important contributions of this study. The 2D-SBM calculates SDF of aerosol in cloud droplets (henceforth we refer the aerosol in cloud droplets to in-cloud aerosol) explicitly. Since the 2D-SBM can calculate size distribution of regenerated aerosols, which is calculated by the parameterization of Feingold et al. (1996) in almost all experiments of this study, it is very useful model to validate the parameterization.

The 2D-SBM calculate size distribution function of in-cloud aerosols based on assumptions that total mass of in-cloud aerosols is not changed during condensation/evaporation and collision/coagulation process, and in-cloud aerosols do not affect the growth process, advection, sedimentation, and diffusion process of clouds.

The assumptions admit us using same calculation scheme of cloud growth process except for collision/coagulation process. When the collision/coagulation process is calculated, number concentration of in-cloud aerosols are conserved. The calculation scheme of Bott (2000) is applied for the calculation of collision/coagulation process in 2D-SBM.

The schematic illustration of the scheme is shown in Fig. A8-1 cited from Bott (2000). The scheme is firstly integrate two-dimensional particle spectrum over the aerosol grid, which yielding a one-dimensional spectrum:

$$f_i = \sum_{l=1}^{N_{aer}} f_{i,l}, \quad \left(l = 1,2,\cdots N_{aer}\right), \tag{A8-11}$$

where N_{aer} is number of aerosol bin (*i.e.* 13 or 17 in this study), and f_i, $f_{i,l}$ is total number concentration of hydrometeors in i-th bin, and number concentration in i-th bin of hydrometeor and l-th bin of aerosols before collision process.

Secondly, the change of hydrometeor's mass are calculated as one-dimensional SBM. The change of mass of i-th bin, j-th bin, k-th bin, and $k+1$-st bin shown as $\Delta g_{c,i}$, $\Delta g_{c,j}$, $\Delta g_{c,k}$,($=g_{c,k}-g_{c,k}(i,j)$) and $\Delta g_{c,k+1}$ ($=g_{c,k+1}+g_{c,k+1}(i,j)$) are calculated by eqs. (A8-4).

Thirdly one-dimensional spectrum is redistributed to two-dimensional spectrum by the procedure shown follow.

The change of total number concentration of two dimensional aerosol-water grid in i-th, j-th, k-th, and $k+1$-st bin are calculated as:

$$\Delta f_{c,i} = \Delta g_{c,i}/m_i, \tag{A8-12a}$$

$$\Delta f_{c,j} = \Delta g_{c,j}/m_j, \tag{A8-12b}$$

$$\Delta f_{c,k} = \Delta g_{c,k}/m_k, \tag{A8-12c}$$

$$\Delta f_{c,k+1} = \Delta g_{c,k+1}/m_{k+1}. \tag{A8-12d}$$

Since in the method the probability for the collision of two drops is assumed to be independent of their aerosol mass, in the two-dimensional aerosol-water grid the total loss of drops $\Delta f_{c,i}$ and $\Delta f_{c,j}$ will be split up in fractions $\Delta f_{c,i,l}(i,j)$ and $\Delta f_{c,j,l}(i,j)$ according to the fraction $\gamma_{i,l}$, and $\gamma_{j,l}$ of particles in grid box (i,l) and (j,l), l=1,2, …., N_{aer}, before the collision process:

$$\begin{aligned} \Delta f_{c,i,l}\left(i,j\right) &= \gamma_{i,l}\Delta f_{c,i}\left(i,j\right) \\ \Delta f_{c,j,l}\left(i,j\right) &= \gamma_{j,l}\Delta f_{c,j}\left(i,j\right). \\ \gamma_{i,l} = \frac{f_{c,i,l}}{f_{c,i}}, \quad \gamma_{j,l} &= \frac{f_{c,j,l}}{f_{c,j}} \end{aligned} \tag{A8-13}$$

Note that $\sum_{l=1}^{N_{aero}} \gamma_{i,l} = 1, \quad i = 1,2, \ldots N_{bin}$. The new drops $\Delta f_{c,k}$ and $\Delta f_{c,k+1}$ is redistributed into grid boxes (k,l) and $(k+1,l)$, l=1,2,….N_{aer}. The collision process of particles with masses (m_i, $m_{a,m}$) with particles (m_j,$m_{a,n}$) yields new particles with masses [m_k,$m'_a(i,j)$] and [m_{k+1},$m'_a(i,j)$] where $m'_a(i,j)=m_{a,m}+m_{a,n}$. The fraction of these particles is given by

$$\Delta f'_k(m,n)=\gamma_{i,m}\ \gamma_{j,n}\Delta f_k$$

$$\Delta f'_{k+1}(m,n)=\gamma_{i,m}\ \gamma_{j,n}\ \Delta f_{k+1}. \qquad \text{(A8.14)}$$

Analogously to the hydrometeors, aerosol number of p-th bin $m_{a,p} < m'_a(i,j) < m_{a,p+1}$ are separated to p-th bin and $p+1$-st bin as:

$$\Delta f_{k,p}(m,n) = (1-c_{a,p})\Delta f'_k(m,n), \qquad \text{(A8-15a)}$$

$$\Delta f_{k+1,p}(m,n) = (1-c_{a,p})\Delta f'_{k+1}(m,n), \qquad \text{(A8-15b)}$$

$$\Delta f_{k,p+1}(m,n) = c_{a,p}\Delta f'_k(m,n), \qquad \text{(A8-15c)}$$

$$\Delta f_{k+1,p+1}(m,n) = c_{a,p}\Delta f'_{k+1}(m,n), \qquad \text{(A8-15d)}$$

with

$$c_{a,p} = \frac{\ln m'_a(i,j) - \ln m_{a,p}}{\ln m_{a,p+1} - \ln m_{a,p}}. \qquad \text{(A8-16)}$$

The scheme of collision/coagulation shown below is based on Bott (2000) and the code of this scheme is downloadable from http://www2.meteo.uni-bonn.de/forschung/gruppen/tgwww/people/index_german.php?memid=2.

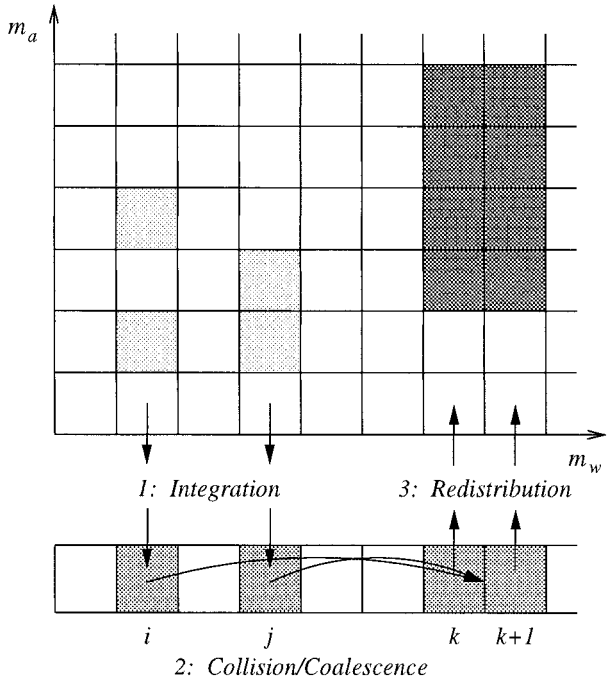

Figure A8-1. Schematic illustration of the method to calculate collision/coagulation by 2D-SBM (Bott et al. 2000)

Appendix A9: Derivation of equations (3-7) and (6-1)

In this section, we describe derivations of eq. (3-7) and (6-1).

A9.1. Derivation of the equation (3-7)

The eq. (3-7) is shown as

$$\tau(h) = \tau_c \left[1 - \left(\frac{h}{H_c} \right)^{5/3} \right], \tag{A9-1}$$

where $\tau(h)$ is COD, τ_c is COT, H_c is geometrical depth of cloud, h is height from cloud top, respectively. This equation is derived from adiabatic-condensation growth model of cloud particles. According to this model, the cloud water content (q_c: g m-3) increase with height h from the cloud bottom in a linear manner as

$$q_c = l_a h \propto h, \tag{A9-2}$$

where l_a is adiabaticy factor. In the adiabatic-condensation growth model, the number concentration of cloud droplets (N_c) is assumed to be constant through the entire cloud layer since the condensation process conserves N_c. The RE (r_{eff}) at each height h is then given as

$$r_{eff} \propto \left(\frac{q_c}{N_c} \right)^{1/3} \propto h^{1/3}. \tag{A9-3}$$

Thus eq. (A9-2) and (A9-3) lead to the cross section σ_c at each height given as

$$\sigma_c \propto \frac{q_c}{r_{eff}} \propto h^{2/3}. \tag{A9-4}$$

The COD $\tau(h)$ from the cloud bottom to the height h then follows from the vertical integral of eq. (A9-4) as

$$\tau(h) = \int_0^h \sigma_c(h')dh' \propto h^{5/3}. \tag{A9-5}$$

Supposing that the total optical thickness of the cloud with geometrical thickness (H_c) is denoted by τ_c, the COD at each height h from the cloud top is therefore given as

$$\tau(h) = \tau_c \left[1 - \left(\frac{h}{H_c} \right)^{5/3} \right]. \tag{A9-6}$$

The eq. (A9-6) is equation (A9-1) and eq. (3-7).

A9.1. Derivation of the equation (6-1)

The derivation of eq. (6-1) is also started from eq. (A9-2). As well as eq. (A9-2), we introduce volume-averaged particle radius r_v given by

$$r_v(h) = \left(\frac{3}{4\pi\rho_w} \frac{q_c}{N_c} \right)^{1/3} = A_{cg}^{1/3} h^{1/3} N_c^{-1/3}, \tag{A9-7}$$

where ρ_w is density of water. $A_{cg}=3l_a/(4\pi\rho_w)$. The RE is related with r_v as $r_e=k_a^{-1/3}r_v$ through the parameter k_a what varies from about 0.67 in continental air masses to about 0.80 in marine air masses (Pontikis and Hicks 1992, Martin et al., 1994). The RE is thus given from r_v as

$$r_e(h) = A_{cg}^{1/3}h^{1/3}(k_aN_c)^{-1/3}. \tag{A9-8}$$

This gives the effective radius at cloud top $h=H$ as

$$r_e(H) = A_{cg}^{1/3}H^{1/3}(k_aN_c)^{-1/3}. \tag{A9-9}$$

In the adiabatic condensation growth model, cloud droplets are considered to grow through condensation process where the number concentration N_c is assumed to be constant. Vertical integration of eq. (A9-2) and eq. (A9-8) over cloud layer of thickness H then leads to the expression for liquid water path W and τ_c as

$$W = \int_0^H q_c\, dh = \frac{1}{2} l_a H^2 , \tag{A9-10}$$

and

$$\tau_c = \frac{Q_{ext}}{\rho_w 4/3}\int_0^H \frac{q_c}{r_{eff}} dh = \frac{3}{5} Q_{ext}\pi A_{cg}^{2/3}\left(k_a N_c\right)^{1/3} H^{5/3} , \tag{A9-11}$$

where Q_{ext} is extinction coefficient. Eqs. (A9-9) and (A-9-11) demonstrate that $r_{eff}(H)$ and τ_c are related through the parameters N_c and H as discussed by previous studies (*e.g.*, Brenguier et al., 2000). The parameter H can be replaced with W since these two quantities are uniquely related through eq. (A9-10); thus eq. (A9-9) and eq. (A9-11) can be rewritten in terms of N_c and W as

$$\begin{aligned} r_{eff}\left(H\right) &= A_{cg}^{1/3}\left(\frac{2W}{l_a}\right)^{1/6}\left(k_a N_c\right)^{-1/3} \\ \tau_c &= \frac{3}{5} Q_{ext}\pi A_{cg}^{2/3}\left(k_a N_c\right)^{1/3}\left(\frac{2W}{l_a}\right)^{5/6} \end{aligned} . \tag{A9-12}$$

These formulas provide theoretical relationships between $r_{eff}(H)$ and τ_c under constant values of N_c and W as

$$\tau_c = \begin{cases} \frac{8}{5}\left(\pi k_a\right)^2 \frac{\rho_w}{l_a} N_c^2 r_{eff}^5 \left(H\right) \cdots \left(N_c = const.\right) \\ \frac{9}{5}\frac{1}{\rho_w}\frac{W}{r_{eff}} \cdots\cdots\cdots \left(W = const.\right) \end{cases} . \qquad \text{(A9-13)}$$

The equations (A9-13) is same as eq. (6-1).

References

Ackermann, A. S., M. P. Kirkpatrick, D. E. Stevens, and O. B. Toon, 2004: The impact of humidity above stratiform clouds on indirect aerosol climate forcing, *Nature*, **432**, 1014-1017.

Ackermann A. S., M. C. van Zanten, B. Stevens, V. Savic-Jovcic, C. S. Bretherton, A. Chlond, J.-C. Golaz, H. Jiang, M. Khairoutdinov, S. K. Krueger, D. C. Lewellen, A. Lock, C.-H. Moeng, K. Nakamura, M. D. Petters, J. R. Snider, S. Weinbrecht, and M. Zulauf, 2009: Large-eddy simulations of drizzling, stratocumulus-topped marine boundary layer. *J. Atmos. Sci.*, **137**, 1083-1110.

Albrecht, B. A., 1989: Aerosols, cloud microphysics, and fractional cloudiness., *Science*, **245**, 1227-1230.

Albrecht, B. A., D. A. Randall, and S. Nicholls, 1988: Observations of marine stratocumulus clouds during FIRE, *Bull. Amer. Meteor. Soc.*, **69**, 618-626.

Albrecht, B. A., C. S. Bretherton, D. Johnson, W. H. Scubert, and A. S. Frisch, 1995: The Atlantic stratocumulus transition experiment-ASTEX, *Bull, Amer. Meteor. Soc.*, **76**., 889-904.

Andrea, M. O., W. Elbert, and S. J. de Mora, 1995: Biogenic sulfur emissions and aerosol over the tropical south Atlantic 3. Atmospheric dimethylsulfide, aerosol and cloud condensation nuclei, *J. Geophys. Res.*, **100**, doi:10.1029/94JD02828

Asano, S., M. Shiobara, and A. Uchiyama, 1995: Estimation of cloud physical parameters from airborne solar spectral reflectance measurements for stratocumulus clouds, *J. Atmos. Sci.*, **52**, 3556-3576.

Ayers, G. P., and J. L. Gras, 1991: Seasonal relatonship between cloud condensation nuclei and aerosol methanesulphonate in marine air, *Nature*, **353**, 834-835.

Berry, E. X., 1967: Cloud droplet growth by collection, *J. Atmos. Sci.*, **24**, 688-701.

Bott, A., 1998: A flux method for the numerical solution of the stochastic collection equation, *J. Atmos. Sci.*, **55**, 2284-2293.

Bott, A., 2000: A flux method for the numerical solution of the stochastic collection equation: extension to two-dimensional particle distributions, *J. Atmos. Sci.*, **57**, 284-294.

Bores, R., and L. D. Rotstayn, 2001: Possible links between cloud optical depth and effective radius in remote sensing observations, *Q. J. R. Meteorol. Soc.*, **127**, 2367-2383.

Brenguier, J.-L., H. Pawlowska, L. Schüller, R. Preusker, J. Fischer, and Y. Fouquart, 2000: Radiative properties of boundary layer clouds: Droplet effective radius versus number concentration. *J. Atmos. Sci.*, **57**, 803-821.

Brenguier, J.-L., H. Pawlowska, and L. Schüller, 2003: Cloud microphysical and radiative properties for parameterization and satellite monitoring of the indirect effect of aerosol on climate, *J. Geophys. Res.*, **108**, D15, 8632, doi:10.1029/2002JD002682

Bretheron, C. S., M. K. Macvean, P. Bechtold, A. Chlond, W. R. Cotton, J. Cuxart, H. Cuijpers, M. Khairoutdinov, B. Kosovic, D. Lewellen, C.-H. Moeng, P. Siebesma, B. Stevens, D. E. Stevens, I. Sykes, and M. C. Wyant, 1999: An intercomparison of radiatively driven entrainment and turbulence in a smoke cloud, as simulated by different numerical models, *Q. J. R. Meteorol. Soc.*, **125**, 391-423.

Bretherton C. S., T. Uttal, C. W. Fairall, S. E. Yuter, R. A. Weller, D. Baumgardner, K. Comstock, R. Wood, and G. B. Raga, 2004: The EPIC 2001 stratocumulus study, *Bull. Amer. Meteor. Soc.*, **85**, 967-977.

Chen, J.-P., and D. Lamb, 1994: Simulation of cloud microphysical and chemical processes using a multicomponent framework. partI: Description of the microphysical model, *J. Atmos. Sci.*, **51**, 2613-2630.

Chlond, A., F. Muller, and I. Sednev, 2004: Numerical simulation of the diurnal cycle of marine stratocumulus during FIRE – And LWS and SCM modeling study, *Quart. J. Roy. Meteor. Soc.*, **130**, 3297-3321.

Choi, I.-J., T. Iguchi, S.-W. Kim, S.-C. Yoon, and T. Nakajima, 2010: Simulation of the aerosol effect on the microphysical properties of shallow stratocumulus clouds over East Asia using a bin-based meso-scale cloud model, *Atmos. Chem. Phys. Discuss.*, **10**, 23449-23495.

Clarke, A. D., J. L. Varner, F. Eisele, R. L. Mauldin, D. Tanner, and M. Litchy, 1998: Particle production in the remote marine atmosphere: Cloud outflow and subsidence during ACE 1, *J. Geophys. Res.*, **103(D13)**, 16379-16409.

Clarke, A. D., S. R. Owens, and J. Zhou, 2006: An ultrafine sea-salt flux from breaking waves: Implications for cloud condensation nuclei in the remote marine atmosphere, *J. Geophys. Res.*, **111**, doi:10.1029/2005JD006565

Deadroff, J. W., 1980: Stratocumulus-capped mixed layers derived from a three-dimensional model. *Boundary-Layer Meteor.*, **18**, 495-527.

Daum, P. H., Y. Liu, R. L. McGraw, Y.-N. Lee, J. Wang, G. Senum, M. Miller, and J. G. Hudson, 2007: Microphysical properties of stratus/stratocumulus clouds during the 2005 marine stratus/stratocumulus experiment (MASE), *J. Geophys. Res.*, submitted.

Dong, X., P. Minnis, G. G. Mace, W. L. Smith Jr., M. Poellot, R. T. Marchand, and A. D. Rapp, 2002: Comparison of stratus cloud properties deduced from surface, GOES, and aircraft data during the March 2000 ARM cloud IOP, *J. Atmos. Sci.*, **59**, 3265-3284.

Dong, X., and G. G. Mace, 2003: Profiles of low-level stratus cloud microphysics deduced from ground-based measurements, *J. Atmos. Oceanic Technol.*, **20**, 42-53.

Dong, X., P. Minnis, B. Xi, S. Sun-Mack, and Y. Chen, 2008: Comparison of CERES-MODIS stratus cloud properties using ground-based measurements at the DOE ARM SGP site., *J. Geophys. Res.*, **113**, D03204, doi:10.1029/2007JD009769

Duynkerke, P. G., H. Zhang, and P. J. Jonker, 1995: Microphysical and turbulent structure of

nocturnal stratocumulus as observed during ASTEX, *J. Atmos. Sci.*, **52**, 2763-2777.

Feingold, G., S. M. Kreidenweis, B. Stevens, and W. R. Cotton, 1996: Numerical simulations of stratocumulus processing of cloud condensation nuclei through collision-coalescence. *J. Geophys. Res.*, **101**, D16, 21391-21402.

Feingold, G., I. Koren, H. Wang, H. Xue, and W. A. Brewer, 2010: Precipitation-generated oscillations in open cellular cloud fields, *Nature*, **466**, doi:10.1038/nature09314.

Matsui, T., H. Masunaga, and R. A. Pielke Sr., 2004: Impact of aerosols and atmospheric thermodynamics on cloud properties within climate system, *Geophys. Res. Lett.*, **31**, 9 L06109, doi:10.1029/2003GL019287.

Han, Q., W. B. Rossow, and A. A. Lacis, 1994: Near-global survey of effective droplet radii in liquid water clouds using ISCCP data, *J. Climate*, **7**, 465-497.

Han, Q., W. B. Rossow, J. Chou, and R. M. Weich, 1998: Global variation of column droplet concentration in low-level clouds, *Geophys. Res. Lett.*, **25**, 1419-1422, doi:10.1029/98GL01095.

Hashino, T., M. Sato, T. Kubota, T. Nasuno, Y. Hagihara, T. Matsui 2011, in Japanese, 能動型衛星観測を用いた全球雲解像モデルの雲微物理棟計量の評価, 日本気象学会 2011 春期大会, B404.

Heintzenberg, J. W. Birmili, A. Wiedensohler, A. Nowak, and T. Tuch, 2004: Structure, variability and persistence of the submicrometre marine aerosol, *Tellus B*, **56**, 357-367

Hong, S. Y., and H. L. Pan, 1996: Nonlocal boundary layer vertical diffusion in a medium-range forecast model., *Mon. Wea. Rev.*, **124**, 2322-2339.

Hudson, J. G., Y. Xie 1999: Vertical distribution of cloud condensation nuclei spectra over the summer time northeast Pacific and Atlantic Ocean, *J. Geophys. Res.*, **104**, D23, 30219-30229.

Iguchi, T., T. Nakajima, A.P. Khain, K. Saito, T. Takemura, and K. Suzuki, 2008: Modeling the

influence of aerosols on cloud microphysical properties in the East Asia region using a mesoscale model coupled with a bin-based cloud microphysics scheme. *J. Geophys. Res.*, **113**, D14215, doi:10.1029/2007JD009774.

Iguchi, T., T. Matsui, X. Li, J. J. Shi, and W.-K. Tao, 2010: Numerical experiment of lake-effect snowstorm in C3VP campaign using the WRF model coupled with spectral bin microphysics., *AGU fall meeting*, A11B0035, San Francisco, USA.

Ikawa, M., and K. Saito, 1991: Description of a non-hydrostatic model developed at the forecast research department of MRI, *Tech. Rep. MRI*, **28**, 238 pp., Meteorol. Res. Inst., Tsukuba, Japan.

IPCC, *Climate Change 2007*, 2007: *The physical science basis*, Solomon, S., D. Win, M. Manning, Z. Chen, M. Marquis, K. B. Averyt, M. Tignor, and H. L. Miller (eds.), Cambridge University Press, 1009pp.

Ivanova, I. T., and H. G. Leighton 2008, Aerosol-cloud interactions in a mesoscale model. part II: sensitivity to aqueous-phase chemistry.Ivano, *J. Atmos. Sci.*, **65**, 309-330.

Katoshevski, D, A. Nenes, and J. H. Seinfeld, 1999: A study of processes governing the maintenance of aerosols in the marine boundary layer, *J. Atmos. Sci.*, **30**, 503-532.

Kawamoto, K., T. Nakajima, and T. Y. Nakajima, 2001: A global determination of cloud microphysics with AVHRR remote sensing. *J. Climate*, **14**, 2045-2068.

Kazil, J., H. Wang, G. Feingold, A. D. Clarke, J. R. Snider, and A. R. Bandy, 2011: Modeling chemical and aerosol processes in the transition from close to open cells during VOCALS-REx, *Atmos. Chem. Phys.*, **11**, 7491-7514.

Kessler, E., 1969: On the distribution and continuity of water substance in atmospheric circulations, *Meteor. Monogr.*, No. 10, 84 pp, Amer. Meteor. Soc.

Khain, A. P., and I. Sednev, 1996: Simulation of precipitation in the eastern Mediterranean coastal

zone using a spectral microphysics cloud ensemble model, *Atmos. Sci.*, **43**, 77-110.

Khain, A. P., M. Ovtchinnikov, M. Pinsky, A. Plkrovsky, and H. Krugliak 2000: Notes on the state-of-the-art numerical modeling of cloud microphysics, *Atmos. Res.*, **55**, 159-224.

Khain, A. P., D. Rosenfeld, and A. Pokrovsky, 2005: Aerosol impact on the dynamics and microphysics of deep convective clouds, *Q. J. R. Meteorol. Soc.*, **131**, 2639-2663

Klein, S. A., D. L. Hartmann 1993: The seasonal cycle of low stratiform cloud, *J. Climate*, **6**, 1587-1606.

Kobayashi, T., and K. Masuda, 2008: Effects of precipitation on the relationships between cloud optical thickness and drop size derived from space-borne measurements, *Geophys. Res. Lett.*, **35**, L24809, doi:10.1029/2008JD009876.

Lebsock, M. D., G. L. Stephens, and C. Kummerow, 2008: Multisensor satellite observations of aerosol effects on warm clouds, *J. Geophys. Res.*, **113**, D15205 doi:10.1029/2008JD009876.

Lohmann, U., G. Tselioudis, and C. Tyler, 2000: Why is the cloud albedo-particle size relationship different in optically thick and optically thin clouds? *Geophys. Res. Lett.*, **27**, 1099-1102.

Long, A. B., 1974: Solutions to the droplet collection equation for polynomial kernels. *J. Atmos. Sci.*, **31**, 1040-1052.

Low, R. D. H., 1969: A generalized equation for the solution effect in droplet growth, *J. Atmos. Sci.*, **26**, 608-611.

Lynn, B. H., A. P. Khain, J. Dudhia, D. Rosenfeld, A. Pokrovsky, and A. Seifert, 2005a: Spectral (bin) microphysics coupled with a mesoscale model (MM5). part I: Model description and first results., *Mon. Wea. Rev.*, **133**, 44-58

Lynn, B. H., A. P. Khain, J. Dudhia, D. Rosenfeld, A. Pokrovsky, and A. Seifert, 2005b: Spectral (bin) microphysics coupled with a mesoscale model (MM5). part II: Simulation of CaPE rain event

with squall line, *Mon. Wea. Rev.*, **133**, 59-71.

Lynn, B., A. Khain, D. Rosenfeld, and W. L. Woodley, 2007: Effect of aerosols on precipitation from orographic clouds, *J. Geophys. Res.*, **112**, D10225, doi:10.1029/2006JD007537

Ma, C.-C., C. R. Mechoso, A. W. Robertson, and A. Arakawa, 1996: Peruvian Stratus clouds and the tropical pacific circulation: a coupled ocean-atmosphere GCM study, *J. Climate.* **9**, 1635-1645.

Mace G. G., R. Marchand, Q. Zhang, and G. Stephens, 2007: Global hydrometeor occurrence as observed by CloudSat: Initial observations from summer 2006. *Geophys. Res. Lett.*, **34**, L09808, doi:10.1029/2006GL029017.

Martin, G. M., D. W. Johnson, and A. Spice, 1994: The measurement and parameterization of effective radius of droplets in warm stratocumulus clouds, *J. Atmos. Sci.*, **31**, 1040-1052.

Matsui T., H. Masunaga, and R. A. Pielke Sr., 2004: Impact of aerosols and atmospheric thermodynamics on cloud properties within the climate system, *Geophys. Res. Lett.*, **31**, L06109, doi:10.1029/2003GL019287.

Matsui, T., H. Masunaga, S. M. Kreidenweis, R. A. Pielke Sr., W.-K. Tao, M. Chin, and Y. J. Kaufman, 2006: Satellite-based assessment of marine low cloud variability associated with aerosol, atmospheric stability, and the diurnal cycle. *J. Geophys. Res.*, **111** D17204, doi:10.1029/2005JD006097.

McCaa, J. R., and C. S. Bretherton, 2004: A new parameterization for shallow cumulus convection and its application to marine subtropical cloud-topped boundary layers. PartII: regional simulations of marine boundary layer clouds., *Mon, Wea. Rev.*, **132**, 883-896.

Mechem, D. B., and Y. L. Kogan, 2003: Simulating the transistion from drizzling marine stratocumulus to boundary layer cumulus with a mesoscale model., *Mon Wea. Rev.*, **131**, 2342-2360.

Mechem, D. B., P. C. Robinson, and Y. L. Kogan, 2006: Processing of cloud condensation nuclei by collision-coalescence in a mesoscale model., *J. Geophys. Res.*, **111**, D18204,

doi:10.1029/2006JD007183.

Mitra S. K., J. Brinkmann, and H. R. Pruppacher, 1992: A wind tunnel study on the drop-to-particle conversion,. *J. Atmos. Sci.*, **23**, 245-256.

Mocko, D. M., and W. R. Cotton, 1995: Evaluation of fractional cloudiness parameterizations for use in mesoscale model., *J. Atmos. Sci.*, **52**, 2884-2901.

Nakajima T., M. Tanaka, 1986: Matrix formulation for the transfer of solar radiation in a plane-parallel scattering atmosphere, *J. Quant. Spectrosc. Radiat. Transfer*, **35**, 13-21.

Nakajima T., M. Tanaka, 1988: Algorithms for radiative intensity calculations in moderately thick atmospheres using a truncation approximation, *J. Quant. Spectrosc. Radiat. Transfer*, **40**, 51-69.

Nakajima, T., and M. D. King, 1990: Determination of the optical thickness and effective particle radius of clouds from reflected solar radiation measurements. Part I: Theory, *J. Atmos. Sci.*, **47**, 1878-1893.

Nakajima, T., M. D. King, J. D. Spinhirne, and L. F. Radke, 1991: Determination of the optical thickness and effective particle radius of clouds from reflected solar radiation measurements. Part II: Marine stratocumulus observations, *J. Atmos. Sci.*, **48**, 728-751.

Nakajima, T., M. Tsukamoto, Y. Tsushima, A. Numaguti, and T. Kimura, 2000: Modeling of the radiative process in an atmospheric general circulation model., *Appl. Opt.*, **39**, 4869-4878.

Nakajima, T., A. Higurashi, K. Kawamoto, and J. E. Penner, 2001: A possible correlation between satellite-derived cloud and aerosol microphysical parameters. *Geophys. Res. Lett.*, **28**, 1171-1174.

Nakajima T. Y. and T. Nakajima, 1995: Wide-area determination of cloud microphysical properties from NOAA AVHRR measurements for FIRE and ASTEX regions. *J. Atmos. Sci.*, **52**, 4043-4059.

Nakajima, Y. T., K. Suzuki, and G. L. Stephens, 2010a: Droplet growth in warm water clouds observed by the A-train. Part I: Sensitivity analysis of the MODIS-derived cloud droplet sizes. *J.*

Atmos. Sci., **67**, 1884-1896.

Nakajima, Y. T., K. Suzuki, and G. L. Stephens, 2010b: Droplet growth in warm water clouds observed by the A-Train. Part II: A multisensory view. *J. Atmos. Sci.*, **67,** 1897- 1907.

Onogi, K., J. Tsutsui, H. Koide, M. Sakamoto, S. Kobayashi, H. Hatsushika, T. Matsumoto, N. Yamazaki, H. Kamahori, K. Takahashi, S. Kadokura, K. Wada, K. Kato, R. Oyama, T. Ose, N. Mannoji, and R. Taira, 2007: The JRA-25 reanalysis, *J. Meteor. Soc. Jpn. I*, **85**, 369-432.

Okamoto, H., S. Iwasaki, M. Yasui, H. Horie, H. Kuroiwa, and H. Kumagai, 2003: An algorithm for retrieval of cloud microphysics using 95-GHz cloud radar and lidar. *J. Geophys. Res.*, **108**, D7, 4226, doi:10.1029/2001JD001225.

Okamoto, H., T. Nishizawa, T. Takemura, H. Kumagai, H. Kuroiwa, N. Sugimoto, I. Matsui, A. Shimizu, A. Kamei, S. Emori, and T. Nakajima, 2007: Vertical cloud structure observed from shipborne radar and lidar: mid-latitude case study during the MR01/K02 cruise of the R/V Mirai. *J. Geophys. Res.*, **112**, D08216, doi:10.1029/2006JD007628,2007

Okamoto, H., T. Nishizawa, T. Takemura, K. Sato, H. Kumagai, Y. Ohno, N. Sugimoto, A. Shimizu, I. Matsui, and T. Nakajima, 2008: Vertical cloud properties in the tropical western Pacific Ocean: Validation of the CCSR/NIES/FRCGC GCM by shipborne radar and lidar. *J. Geophys. Res.*, **113**, D24213, doi:10.1029/2008JD009812.

Platnick, S., 2000: Vertical photon transport in cloud remote sensing problems. *J. Geophys. Res.*, **105**, 22919-22935.

Pontikis, C. A., and E. Hicks, 1992: Contribution to the cloud droplet effective radius parameterization, *Geophys. Res. Lett.*, **19**, 2227-2230.

Pruppacher, H., and J. D. Klett, 1997: *Microphysics of Clouds and Precipitation*. 2nd ed., Springer, New York, 954 pp.

Randall, D. A., J. A. Coakley, Jr., C. W. Fairall, R. A. Kropfli, and D. H. Lenschow,

1984: Outlook for research on subtropical marine stratiform clouds. *Bull. Amer. Meteor. Soc.*, **65**, 1290-1301.

Remer, L. A., Y. J. Kaufman, D. Tanre, S. Mattoo, D. A. Chu, J. V. Martins, R.-R. Li, C. Ichoku, R. C. Levy, R. G. Kleidman, T. F. Eck, E. Vermote, and B. N. Holben, 2005: The MODIS aerosol algorithm, products and validation. *J. Atmos. Sci.*, **62**, 947-973.

Rogers R. R., and M. K. Yau 1989: *A short course in cloud physics*, 3rd ed., 293 pp. Pergamon Press, Oxford, U.K.

Rosenfeld, D., 2000: Suppression of rain and snow by urban and industrial air pollusion, *Science*, **287**, 1793-1796.

Rosenfeld, D., and G. Gutman, 1994: Retrieving microphysical properties near the tops of potential rain clouds by multispectral analysis of AVHRR data, *Atmos. Res.*, **34**, 259-283.

Rossow, W. B., and R. A. Schiffer, 1999: Advances in understanding cloud from ISCCP, *Bull. Amer. Meteorol. Soc.*, **80**, 2261-2287.

Saito, K., 1997: Semi-implicit fully compressible version of the MRI mesoscale nonhydrostatic model –Forecast experiment of the 6 August 1993 Kagoshima torrential rain--, *Geophys. Mag. Ser.* 2, **2**, 109-137.

Saito, K., T. Fujita, Y. Yamada, J. Ishida, Y. Kumagai, K. Aranami, S. Ohmori, R. Nagasawa, S. Kumagai, C. Muroi, T. Kato, H. Eito, and Y. Yamazaki, 2006: The operational JMA nonhydrostatic mesoscale model. *Mon. Wea. Rev.*, **134**, 1266-1298.

Sato, Y., T. Nakajima, K. Suzuki, and T. Iguchi, 2009: Application of a Monte Carlo integration method to collision and coagulation growth processes of hydrometeors in a bin-type model. *J. Geophys. Res.*, **114**, D09215, doi:10.1029/2008JD011247.

Sato, Y., K. Suzuki, T. Iguchi, I.-J. Choi, H. Kadowaki, and T. Nakajima, 2012a: Characteristics of correlation statistics between droplet radius and optical thickness of warm clouds simulated by a

three-dimensional regional-scale spectral bin microphysics cloud model, *J. Atmos. Sci.*, **69**, 484-503.

Sato, Y., T. Y. Nakajima, and T. Nakajima, 2012b: Investigation of the vertical structure of warm cloud microphysical properties using the cloud evolution diagram, CFODD, simulated by three-dimensional spectral bin microphysical model., *J. Atmos. Sci.*, accepted.

Savic-Jovcic, V., and B. Stevens, 2008: The structure of mesoscale organization of precipitating stratocumulus. *J. Atmos. Sci.*, **65**, 1587-1605.

Sekiguchi, M., and T. Nakajima, 2008: A k-distribution-based radiation code and its computational optimization for n atmospheric general circulation model., *J. Quant. Spectrosc. Radiat. Transfer.*, **109**, 2779-2793.

Squires, P. (1956), The micro-structure of cumuli in marine and continental air, *Tellus*, **8**, 443-444.

Stephens, G. L., D. G. Vane, R. J. Boain, G. G. Mace, K. Sassen, Z. Wang, A. J. Illingworth, E. J. O'Connor, W. B. Rossow, S. L. Durden, S. D. Miller, R. T. Austin, A. Benedetti, C. Mitrescu, and The CloudSat Science Team, 2002: The CloudSat mission and the A-Train. *Bull. Amer. Meteor. Soc.*, **83**, 1771-1790.

Stephens, G. L., 2005: Cloud feedbacks in the climate system: a critical review, *J. Climate*, **18**, 237-273.

Stephens, G. L., D. G. Vane, S. Tanelli, E. Im, S. Durden, M. Rokey, D. Reinke, P. Partain, G. G. Mace, R. Austin, T. L'Ecuyer, J. Haynes, M. Lebsock, K. Suzuki, D. Waliser, D. Wu, J. Kay, A. Gettelman, Z. Wang, and R. Marchand, 2008: The CloudSat mission: performance and early science after the first year of operation. *J. Geophys. Res.*, **113**, doi:10.1029/2008JD009982.

Stevens, B., C.-H. Moeng, P. P. Sullivan, 1999: Large-eddy simulations of radiatively driven convection: Sensitivities to the representation of small scales. *J. Atmos. Sci.*, **55**, 3963-3984.

Stevens, B., D. H. Lenschow, G. Vali, H. Gerver, A. Bandy, B. Blomquist, J.-L. Brenguier, C. S. Bretherton, F Burnet, T. Campos, S. Chai, I. Faloona, D. Friesen, S. Haimov, K. Laursen, D. K.

Lilly, S. M. Loehrer, S. P. Malinowski, B. Morley, M. D. Petters, D. C. Rogers, L. Russell, V. Savic-Jovcic, J. R. Snider, D. Straub, M. J. Szumowski, H. Takagi, D. C. Thornton, M. Tschudi, C. Twohy, M. Wetzel, and M. C. van Zanten, 2003, Dynamics and chemictry of marine stratocumulus DYCOMS-II, *Bull. Amer. Meteor. Soc.*, **84**, 579-593.

Stevens, B., C.-H. Moeng, A. S. Ackermann, C. S. Bretherton, A. Chlond, S. de Roode, J. Edwartd, J.-C., Golaz, H. Jiang, M. Khairoutdinov, M. P. Kirkpatrick, D. C. Lewellen, A. Lock, F. Muller, D. E. Stevens, E. Whelan, and P. Zhu, 2005: Evaluation of large-eddy simulations via observations of nocturnal marine stratocumulus. *Mon. Wea. Rev.*, **133**, 1443-1462.

Sun, W. Y. and C. Z. Chang, 1986: Diffusion model for a convective layer. Part I: Numerical simulation of convective boundary layer, *J. Climate Appl. Meteor.*, **25**, 1445-1453.

Suzuki, K., 2004: A study on numerical modeling of cloud microphysics for calculating the particle growth process (in Japanese), Univ. Tokyo, doctoral dissertation, 136 pp

Suzuki, K., T. Nakajima, A. Numaguti, T. Takemura, K. Kawamoto, and A. Higurashi, 2004: A study of the aerosol effect on a cloud field with simultaneous use of GCM modeling and satellite observation. *J. Atmos. Sci.*, **61**, 179-194.

Suzuki, K., T. Nakajima, T. Y. Nakajima, and A. Khain, 2006: Correlation pattern between effective radius and optical thickness of water clouds simulated by a spectral bin microphysics cloud model, *SOLA*, **2**, doi:10.2151/sola.2006-030.

Suzuki, K., T. Nakajima, T. Y. Nakajima, and A. P. Khain, 2010a: A study of microphysical mechanisms for correlation patterns between droplet radius and optical thickness of warm clouds with a spectral bin microphysics model, *J. Atmos. Sci.*, **67**, 1126-1141.

Suzuki, K., T. Nakajima, T. Y. Nakajima, and G. L. Stephens, 2010b: Effect of the droplet activation process on microphysical properties of warm clouds, *Environ. Res. Lett.*, **5**, doi:10.1088/1748-9362/5/2/024012

Suzuki, K., T. Y. Nakajima, and G. L. Stephens, 2010c: Particle growth and drop collection

efficiency of warm clouds as inferred from joint CloudSat and MODIS observations. *J. Atmos. Sci.*, **67**, 3019-3032.

Takahashi, T., and T. Kawano, 1998: Numerical sensitivity study of rainband precipitation and evolution, *J. Atmos. Sci.*, **55**, 57-87

Takahashi, T., and K. Shimura, 2004: Tropical rain characteristics and microphysics in a three-dimensional cloud model, *J. Atmos. Sci.*, **61**, 2817-2845.

Takemura, T., T. Nozawa, S. Emori, T. Y. Nakajima, and T. Nakajima, 2005: Simulation of climate response to aerosol direct and indirect effects with aerosol transport-radiation model. *J. Geophys. Res.*, **110**, D02202, doi:10.1029/2004JD005029.

Twomey, S., 1974: Pollution and the planetary albedo., *Atmos. Environ.*, **8**, 1251-1256.

Uchida, J., C. S. Bretherton, and P. N. Blossey, 2010: The sensitivity of stratocumulus-capped mixed layers to cloud droplet concentration: do LES and mixed-layer models agree?, *Atmos. Chem. Phys.*, **10**, 4097-4109.

van Zanten, M. C., B. Stevens, G. Vali, and D. H. Lenschow, 2005: Observations of drizzle in nocturnal marine stratocumulus, *J. Atmos. Sci.*, **62**, 88-106.

van Zanten, M. C., and B. Stevens, 2005: Observation of the structure of heavily precipitating marine stratocumulus, *J. Atmos. Sci.*, **62**, 4327-4342.

Wang, H., and G. Feingold, 2009a: Modeling mesoscale cellular structures and drizzle in marine stratocumulus part I: Impact of drizzle on the formation and evolution of open cells, *J. Atmos. Sci.*, **66**, 3237-3256.

Wang, H., and G. Feingold, 2009b: Modeling mesoscale cellular structures and drizzle in marine stratocumulus part II: The microphysics and dynamics of the boundary region between open and closed cells, *J. Atmos. Sci.*, **66**, 3257-3275.

Wang, H., P. J. Rasch, and G. Feingold, 2011: Manipulanting marine stratocumulus cloud amount and albedo: a process-modeling study of aerosol-cloud-precipitation interactions in response to injection of cloud condensation nuclei, *Atmos. Chem. Phys.*, **11**, 4237- 4249.

Wang, S., B. A. Albrecht, and P. Minnis, 1993: A regional simulation of marine boundary-layer clouds., *J. Atmos. Sci.*, **50**, 4022-4043.

Winker, D. M., J. Pelon, and M. P. McCormick, 2003: The CALIPSO mission; Spaceborne lidar for observation of aerosols and clouds. *Lidar Remote Sensing for Industry and Environment Monitoring III*, U. N. Singh, T. Itabe, and Z. Liu, Eds., International Society for Optical Engineering (SPIE Proceedings, Vol. 4893), doi:10.1117/12466539.

Winker, D. M., W. H. Hunt, and M. J. McGill, 2007: Initial performance assessment of CALIOP. *Geophys. Res. Lett.*, **34**, L19803, doi:10.1029/2007GL030135.

Xue, L., A. Teller, R. Rasmussen, I. Geresdi, and Z. Pan, 2011: Effects of aerosol solubility and regeneration on warm-phase orographic clouds and precipitation simulated by a detailed bin microphysical scheme, *J. Atmos. Sci.*, **67**, 3336-3354.

Yamada, Y., 2003: Cloud microphysics (in Japanese), in *The JMA Non-hydrostatic Model*, *Annu. Rep.*, **49**, pp. 52-76, Jpn. Meteorol. Agency., Tokyo.